Electronic Supplementary Information (ESI) for Chemical Science.
This journal is ©The Royal Society of Chemistry 2015

Supplemental Information

From a unique Fe_2P_3 complex to FeP nanoparticles acting as efficient bifunctional electrocatalysts for water-splitting

Shenglai Yao,[‡ a] Viktoria Forstner,[‡ a] Prashanth W. Menezes,[‡ a] Chakadola Panda,[‡a] Stefan Mebs,[b] Eva M. Zolnhofer,[c] Matthias E. Miehlich,[c] Tibor Szilvási,[d] Nanjundan Ashok Kumar,[e] Michael Haumann,[b] Karsten Meyer,*[c] Hansjörg Grützmacher*[f] and Matthias Driess*[a]

[a] *Department of Chemistry: Metalorganics and Inorganic Materials, Technische Universität Berlin, Strasse des 17. Juni 135, Sekr. C2, D-10623 Berlin, Germany. E-mail: matthias.driess@tu-berlin.de.* [b] *Department of Physics, Freie Universität Berlin, Arnimallee 14, D-14195 Berlin, Germany.* [C] *Department of Chemistry and Pharmacy, Friedrich-Alexander-University Erlangen-Nürnberg (FAU), Egerlandstrasse 1, 91058 Erlangen, Germany. E-mail: karsten.meyer@fau.de.* [d] *Department of Chemical & Biological Engineering, University of Wisconsin—Madison, 1415 Engineering Drive, 53706, Madison, WI, USA.* [e] *School of Chemical Engineering, The University of Queensland, St Lucia, Brisbane, 4072. Australia.* [f] *Department of Chemistry and Applied Biosciences, ETH Zürich, Vladimir-Prelog Weg 1, Hönggerberg, CH-8093, Zürich. E-mail: hgruetzmacher@ethz.ch*

Content

A. General Considerations

Chemical synthesis experiments and manipulations were carried out under dry oxygen-free nitrogen using standard Schlenk techniques or in an MBraun inert atmosphere drybox containing an atmosphere of purified nitrogen. Solvents were dried by standard methods and freshly distilled prior to use. Doubly distilled water has been used throughout the experiments. The starting material **1** was prepared according to literature procedures.[1] Potassium hydroxide (KOH, 1M) and oleylamine ($CH_3(CH_2)_7CH=CH(CH_2)_7CH_2NH_2$, b.p. ~350°C) was obtained from Sigma Aldrich whereas ruthenium oxide (RuO_2) and iridium oxide (IrO_2) was purchased from Alfa Aesar. The solution NMR spectra were recorded on Bruker Spectrometers ARX 200 and AV 400 with residual solvent signals as internal reference (^1H). High-resolution ESI-MS were measured on a Thermo Scientific LTQ *orbitrap* XL. IR spectra were measured from powder samples inside a nitrogen filled glovebox using a Thermofisher Nicolet iS5 IR Spectrometer (ATR-Diamond) and the OMNIC software (Version 9.3.30) for data acquisition. Solution magnetic susceptibilities were determined by the Evans method.[2,3] PXRD patterns were obtained on a Bruker AXS D8 advanced automatic diffractometer equipped with a position-sensitive detector (PSD) and a curved germanium (111) primary monochromator using Cu Kα radiation (λ = 1.5418 Å). The structural model of the material was drawn using the DIAMOND program version 3.0. ICP-AES was carried out in a Thermo Jarrell Ash Trace Scan analyzer. The samples were digested in aqua regia (electrolytes were used directly in the case of electrochemical measurements) and the average of three reproducible independent experiments has been presented. SEM was carried out on a Hitachi SU8030 microscope with integrated TEAM EDX and a DISS 5 imaging system as well as on a Zeiss DSM 982 GEMINI with integrated EDAX EDX and a point electronic imaging system. TEM measurements were carried out on a JEOL 2100 equipped with an EDX at an acceleration voltage of 200 kV. The quantification of the material was also estimated by the elemental analyses (CHN) that were performed on a Flash EA 112 Thermo Finnigan elemental analyzer. FTIR was studied using a BIORAD FTS 6000 FTIR spectrometer under attenuated total reflection (ATR) conditions. The data were recorded in the range of 400–4000 cm^{-1} with the average of 32 scans at 4 cm^{-1} resolution.

Single-Crystal X-ray Structure Determinations: Crystals were each mounted on a glass capillary in perfluorinated oil and measured in a cold N_2 flow. The data was collected on an Oxford Diffraction SuperNova, Single source at offset, Atlas at 150 K (Cu-Kα radiation, λ = 1.54184 Å). The structures were solved by direct methods and refined on F^2 with the SHELX-97 software package.[4] The positions of the H atoms were calculated and considered isotropically according to a riding model. The P_3 moieties in both structures are equally disordered over two orientations. The structure of **3** contains a disordered cation $[K(thf)_6]^+$ and a disordered free THF molecule. Thus, restraints were used in the refinement. CCDC 1588191 (**2**) and 1588192 (**3**) contain the supplementary crystallographic data for this paper. The data can be obtained free of charge via www.ccdc.cam.ac.uk/data_request/cif, or by emailing data_request@ccdc.cam.ac.uk, or by contacting The Cambridge Crystallographic Data Centre, 12, Union Road, Cambridge CB2 1EZ, UK; fax: +44 1223 336033.

^{57}Fe Mössbauer Spectroscopy. Mössbauer data was recorded on a WissEl spectrometer (MRG-500) at 77 K with alternating constant acceleration and 0.8 GBq ^{57}Co/Rh γ-source. The minimum experimental line width was 0.24 mms^{-1}. The temperature of the samples was controlled by an MBBC-HE0106 MÖSSBAUER He/N_2 cryostat within an accuracy of ±0.3 K Isomer shifts are quoted relative to iron metal at 300K. Mössbauer data were analyzed and simulated using the software "mcal" and "mf" written by E.Bill (mail: ebill@gwdg.de, MPI for Chemical Energy Conversion, Mülheim an der Ruhr).

Magnetic Susceptibility Measurement: Magnetism data of crystalline, finely powdered samples (16 – 18 mg), contained within a polycarbonate gel capsule, were recorded with a Quantum Design MPMS–XL SQUID magnetometer. DC magnetization data were collected in the temperature range of 2 – 300 K with an applied DC field of 1 T. Values of the magnetic susceptibility were corrected for core diamagnetism of the sample estimated using tabulated Pascal's constants.[5] Magnetic susceptibility data were analyzed

and simulated using the julX program written by E. Bill (MPI for Chemical Energy Conversion, Mülheim an der Ruhr).

EPR Measurement: EPR spectra were recorded on a JEOL continuous wave spectrometer JES-FA200 equipped with an X-band Gunn oscillator bridge, a cylindrical mode cavity, and a helium cryostat. The sample was freshly dissolved in dry toluene in an approximately 1 mM concentration in an air-tight J. Young quartz EPR tube. The solution in the tube was frozen in liquid nitrogen upon exiting the glovebox and kept frozen until measured. The spectrum was measured with the following parameters: Temperature 7 K, frequency 8.95148 GHz, modulation amplitude 1.0 mT, microwave power 1.0 μW, modulation frequency 100 kHz, time constant 0.1 s. Analysis and simulation of the data was performed using the software "eview" and "esim" written by E. Bill (mail: ebill@gwdg.de, MPI for Chemical Energy Conversion, Mülheim an der Ruhr).

X-ray absorption spectroscopy. XAS data at the Fe K-edge were collected at beamline KMC-3 at BESSY (Berlin) using a standard set-up as previously described (double-crystal Si[111] monochromator, 13-element energy-resolving germanium detector (Canberra) for X-ray fluorescence detection, samples held in a liquid-helium cryostat (Oxford) at 20 K).[6] Four monochromator scans on separate sample spots (beam size about 5 horizontal x 1 vertical mm^2 set by slits) were collected on powder (microcrystalline) samples of the compounds, which were diluted by grinding with boron nitrite (1:10 w/w) in an anaerobic glove box and filled into Kapton-covered acrylic glass holders. X-ray absorption near edge structure (XANES) and extended X-ray absorption fine structure (EXAFS) spectra were averaged after detector dead-time and sample self-absorption correction (using transmission spectra) of the fluorescence[7] and processed with in-house software as described earlier.[8] EXAFS simulations were carried out with in-house programs and using phase functions calculated with FEFF9.[9]

Density functional theory. Starting from the crystallographic coordinates of **2** and **3**, the molecular structures were optimized in the gas phase by DFT computations at the TPSSh/TZVP[10,11] theory level employing the Gaussian09[12] software package. Prior to geometric relaxation, anti-ferromagnetic coupling was assigned by definition of adequate fragments. The resulting formatted checkpoint files were used to compute the spin density distribution with the cubegen subroutine of Gaussian09. The wavefunction files were used for a topological analysis of the electron density (ED) following the atoms-in-molecules (AIM) space-partitioning scheme with AIM2000,[13] as well as for an analysis of the reduced ED gradient, following the non-covalent interactions indicator (NCI)[14] method with the program nciplot.[14] The optimized coordinates were used as input for time-dependent DFT (TDDFT) computations at the same theory level with ORCA3.0.3[15] to derive theoretical XAS spectra and for conventional DFT calculations to derive Mayer bond orders (MBO)[16] and unrestricted Hartree-Fock corresponding orbitals (UCO).[17] Cube files containing difference densities and corresponding orbitals were generated with the orca_plot subroutine of ORCA3.0.3[15] and, like the spin densities, displayed with ChemCraft (available at https://www.chemcraftprog.com). AIM topologies were displayed with AIM2000[13] and NCI iso-surfaces with MolIso.[18]

X-ray photoelectron spectroscopy (XPS): The XPS measurements on the thin films of FeP were conducted on a Kratos Axis Ultra X-ray photoelectron spectrometer (Karatos Analytical Ltd., Manchester, U.K.) using an Al Kα monochromatic radiation source (1486.7 eV) with 90° takeoff angle (normal to analyzer). The vacuum pressure in the analyzing chamber was kept at 2×10^{-9} Torr. The XPS spectra were collected for C 1s, O 1s, Fe 2p, and P 2p levels with pass energy 20 eV and step 0.1 eV. The binding energies were calibrated relative to the C 1s peak energy position as 285.0 eV. Data analyses were carried out using Casa XPS (Casa Software Ltd.) and the Vision data processing program (Kratos Analytical Ltd.).

Electrophoretic deposition of FeP on the electrode substrate

The FeP powder material was taken in a mixture of iodine and acetone and sonicated for 1 h. By applying a potential difference of 10 V the material was electrophoretically deposited on a 1 × 1 cm^2 area of nickel foam (NF, Racemat BV) The final sample loading on each NF after 2 min of deposition period was ~ 1 $mg(cm)^{-2}$.

Electrochemical measurements

(a) Electrochemistry of the molecular precursors: Cyclic voltammetry (CV) measurements of **2** were carried out at 295 K by using a Biologic SP-150 potentiostat and a three-electrode set-up. Pt-wire was used as an auxiliary electrode, as a working electrode a freshly polished glassy carbon disc (3 mm diameter) and as a pseudo-reference electrode, Ag/Ag^+ was used. All cyclic voltammograms were referenced against the Cp_2Fe/Cp_2Fe^+ (Fc/Fc^+) redox couple which was used as an internal standard. As an electrolyte, 0.3 M solutions of $[Bu_4N]PF_6$ in THF were used. The iR-drop was determined and compensated by using the impedance measurement technique implemented in the EC-Lab Software V10.44.

(b) Electrocatalysis of FeP: A typical catalytic run was conducted in a single compartment three-electrode (catalyst deposited on NF served as working electrode, Pt wire as the counter electrode and Hg/HgO as the reference electrode) electrochemical cell in 1 M KOH using a potentiostat (SP-200, BioLogic Science Instruments) controlled by the EC-Lab v10.20 software package. Cyclic voltammetry (CV) and linear sweep voltammetry (LSV) were carried out with iR compensation of 80% was applied. The potentials presented in this work were referenced to the reversible hydrogen electrode (RHE) through RHE calibration, and in 1 M KOH at pH 14, $E(RHE) = E(Hg/HgO) + 0.098\ V + (0.059 \times pH)\ V$. The chronoamperometric (CA) measurements were performed in aqueous 1 M KOH at selected constant potentials vs. RHE (maintaining a current density of 10 $mAcm^{-2}$).

The electrochemically active surface area (ECSA) of FeP catalyst was attained by determining electrochemical double-layer capacitance, C_{dl}, which was calculated from CV curves recorded in a potential range with no Faradaic current at different scan rates from 10 to 200 mVs^{-1}(cycled between 0.92

and 1.02 V vs RHE). The anodic charging currents measured at 0.97 V vs RHE was plotted as a function of the scan rate and from the slope, C_{dl} was obtained.[19–22] The ECSA of a catalyst was then calculated using ECSA = C_{dl} / C_s where C_s is the specific capacitance of the material per unit area under identical electrolyte conditions. For our estimation, we have used a specific capacitance C_s of 1.7 mFcm^{-2} based on the literature reported values of NF in 1 M KOH solution.[23]

Electrochemical impedance spectroscopy (EIS) measurements were performed over a frequency range from 100 kHz to 1 mHz at 1.5 V vs RHE to attain the Nyquist plots. The impedance spectra were fitted using an equivalent RC circuit model.[19–22] The charge transfer resistance (R_{ct}) was then calculated from the diameter of the semicircle in the Nyquist plots.

The overall water-splitting reaction was achieved in a two-electrode electrochemical cell by using catalysts deposited on NF as anode and cathode and the CA experiments were conducted similarly to HER and OER.

Gas chromatographic analysis

An Agilent 7890A gas chromatograph (GC) was used to determine the hydrogen and oxygen content in the headspace of the electrochemical cell. The GC was equipped with a carboxen-1000 column and a thermal conductivity detector (TCD). The carrier gas was argon (Ar).

B. Synthesis and Characterization of 2-4

Synthesis of 2:

A Schlenk flask was loaded with $L^{H}FeCl_2Li(THF)_2$ (3.45 g, 5.17 mmol) and [Na(OCP)(dioxane)$_{2.5}$] (1.56 g, 5.17 mmol). 100 mL toluene was added to the Schlenk flask at room temperature under stirring. The reaction mixture turned brown immediately and was stirred overnight. Filtration over a G4 glass frit afforded a brown solution which was concentrated and cooled to -30°C. **2** crystallised from the solution after 2 days as dark brown crystals (0.88 g, 0.90 mmol, 52 % b). The IR spectrum of the mother liquor of

2 shows five bands at 2041, 2006, 1968, 1958, and 1925 cm^{-1}, indicative of the formation of $L^{H}Fe(CO)_3$ and $L^{H}Fe(CO)_2$ as side products.[24]

Analytic data of 2

M.p. 256 °C (decomp.). HR ESI-MS (Ion spray voltage 5kV, flow rate 5µL/*min*, in THF): m/z: calcd for $[M]^+$ ($C_{54}H_{74}N_4Fe_2P_3$): 983.38197, found: 983.38209. Elemental analysis (%): calcd for $C_{54}H_{74}N_4Fe_2P_3$: C, 65.93; H, 7.58; N, 5.69. Found: C, 65.26; H, 7.41; N, 5.48. μ_{eff} (Evans, C_6D_6, 298 K) 4.41 μ_B. IR (ART-Diamond, cm^{-1}): ν = 699 (w), 737 (m), 752(m), 733(m), 798 (w), 932 (w), 969 (w), 1057 (w), 1094 (w), 1140 (w), 1178 (w), 1255 (w), 1293 (s), 1321 (w), 1339 (w), 1360 (w), 1380 (w), 1439 (s), 1460 (w), 1503 (m), 1559(m), 2864 (w), 2922 (w), 2957 (m), 3058 (w). UV-Vis (THF): 330 nm (22000 L mol^{-1} cm^{-1}), 420 nm (4400 L mol^{-1} cm^{-1}).

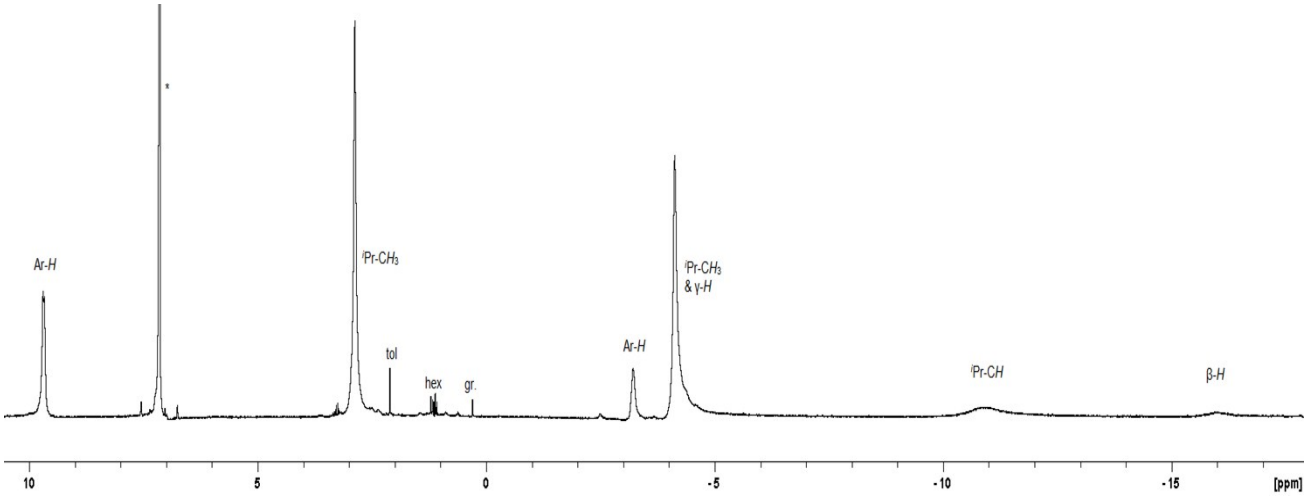

Figure S1. ^1H NMR spectrum of **2** (C_6D_6, 400 MHz): δ/ppm = -15.92 (s, 2H, β-*H*); -10.83 (s, 4H, ^{i}Pr-C*H*); -4.11 (s, 13H, ^{i}Pr-C*H*$_3$ und γ-*H*); -3.19 (t, $^3J_{HH}$ = 6.2 Hz, 2H, Ar-*H*); 2.88 (s, 12H, ^{i}Pr-C*H*$_3$); 9.67 (d, $^3J_{HH}$ = 6.2 Hz, 4H, Ar-*H*).

Synthesis of 3

A Schlenk flask was loaded with **2** (0.26 g, 0.26 mmol) and KC_8 (0.037 g, 0.26 mmol). 30 mL THF was added to the Schlenk flask at room temperature under stirring. The reaction mixture was stirred for 2 h and the coluor of the solution turned dark green. Filtration over a G4 glass frit afforded a dark green solution which was concentrated and cooled to -30°C. **3** crystallised from the solution after 4 days as dark green crystals (0.32 g, 0.22 mmol, 86 %).

Analytic data of 3

M.p. 214 °C (decomp.). Elemental analysis (%): calcd for $C_{78}H_{122}N_4Fe_2P_3KO_2$: C, 64.36; H, 8.45; N, 3.85. Found: C, 64.02; H, 8.21; N, 3.48. μ_{eff} (Evans, THF-D_8, 298 K) 4.28 μ_B. IR (ART-Diamond, cm^{-1}): ν = 600 (w), 726 (w), 752(m), 773(w), 799 (w), 896 (w), 1052 (m), 1093 (w), 1135 (w), 1205 (w), 1244 (w), 1303 (s), 1323 (w), 1357 (w), 1378 (w), 1441 (s), 1500 (m), 1553(w), 2861 (w), 2922 (w), 2952 (m), 3059 (w). UV-Vis (THF): 318 nm (56000 L mol^{-1} cm^{-1}), 472 nm (12000 L mol^{-1} cm^{-1}), 630 nm (540 L mol^{-1} cm^{-1}).

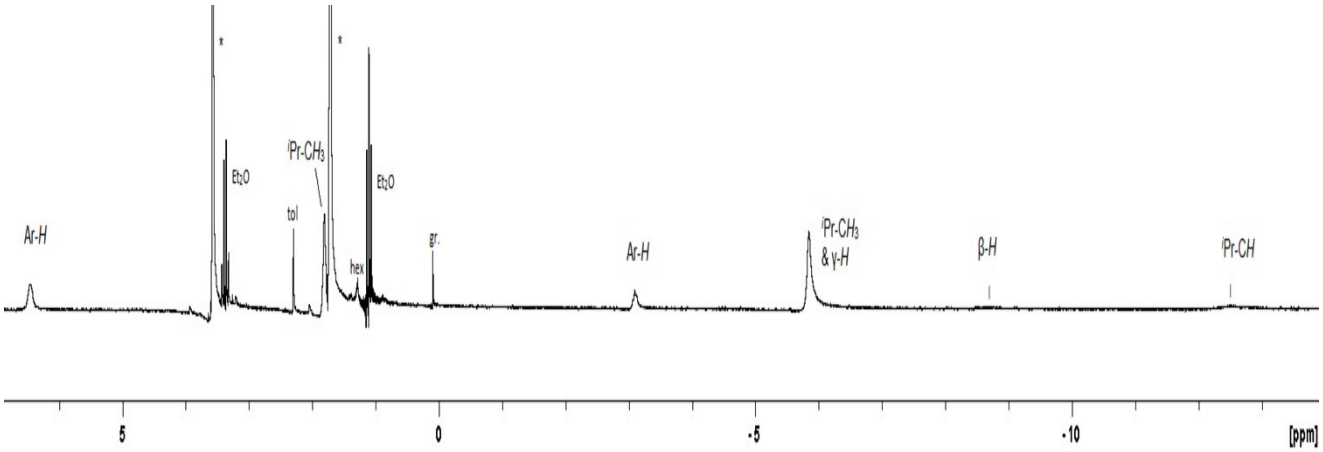

Figure S2. ^{1}H NMR of **3** (, THF-D_8, 200 MHz): δ/ppm = -12.50 (s, 4H, ^{i}Pr-C*H*); -8.66 (s, 2H, β-*H*); -5.85 (s, 13H, ^{i}Pr-C*H*$_3$ und γ-*H*); -3.10 (t, $^3J_{HH}$ = 6.1 Hz, 2H, Ar-*H*); 2.30 (s, 12H, ^{i}Pr-C*H*$_3$); 6.46 (m, 4H, Ar-*H*).

Synthesis of 4

A Schlenk flask was loaded with **2** (0.48 g, 0.49 mmol) and KC_8 (0.09 g, 0.67 mmol). 40 mL THF was added to the Schlenk flask at room temperature under stirring. The reaction mixture was stirred for 2 h and the coluor of the solution turned dark green. Filtration over a G4 glass frit afforded a dark green solution, into which ^{n}Bu$_4$NCl (0.14 g , 0.49 mmol) was added. After 18 h stirring at room temperature, volatiles were removed in vacuo and the residue was dissolved with 70 mL DME. The volume of the solution was reduced to ca. 15 mL before the solution was cooled to -30 °C for 48 h to afford **4** as dark green crystals (0.37 g, 0.29 mmol, 60 %). X-ray single crystal diffraction analysis unambiguously showed that the anion of **4a** is identical to that of **3a** and the cation can also be identified as [^{n}Bu$_4$N]$^+$.

Unfortunately, the quality of the single crystals could not provide crystallographic data for a satisfying refinement.

Analytic data of 4

M.p. 196 °C (decomp.). μ_{eff} (Evans, THF-D_8, 298 K) = 4.28 μ_B. HR ESI-MS (Ion spray voltage 5kV, flow rate 5µL/*min*, in THF) m/z: positive ion mode, calcd for the cation $[^nBu_4N]^+$ ($C_{16}H_{36}N$): 242.28423, Found: 242.28494; negative ion mode, calcd for the anion [M - $^nBu_4N]^-$ ($C_{54}H_{74}N_4Fe_2P_3$): 983.38197, Found: 983.38647.

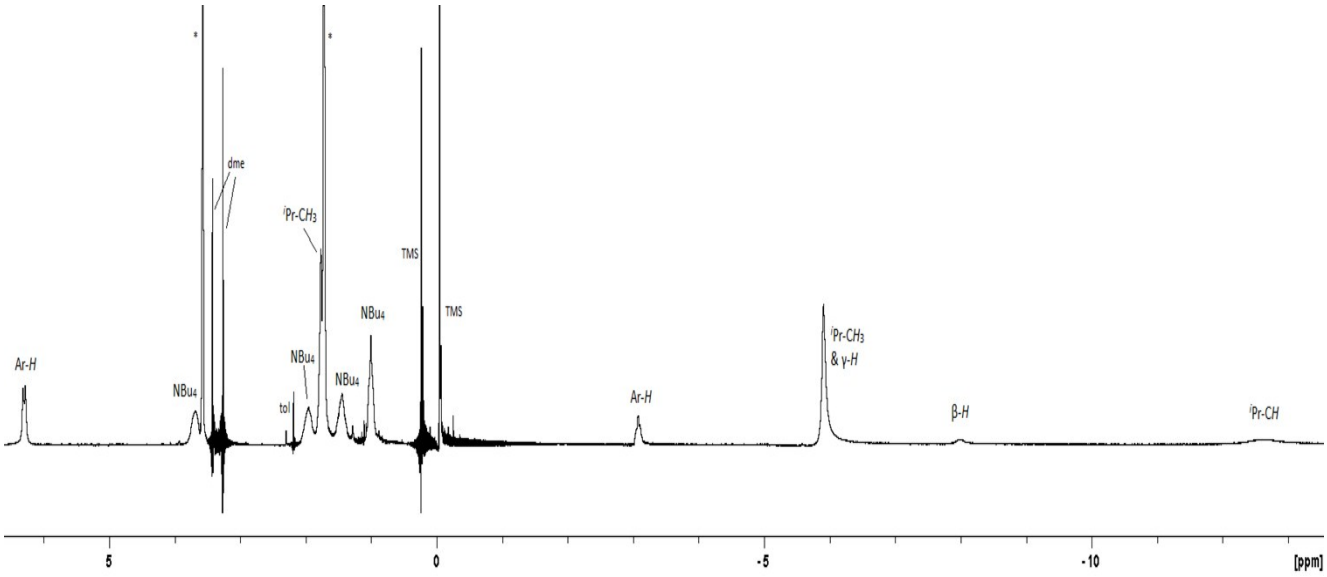

Figure S3. ^{1}H NMR of **4** (, THF-D_8,+TMS, 200 MHz): δ/ppm =-12.59 (s, 4H, ^{i}Pr-C*H*); -7.95 (s, 2H, β-*H*); -5.91 (s, 13H, ^{i}Pr-CH_3 und γ-*H*); -3.07 (t, $^3J_{HH}$ = 6.4 Hz, 2H, Ar-*H*); 1.04 (NBu$_4$-*H*); 1.49 (NBu$_4$-*H*); 1.77 (s, 12H, ^{i}Pr-CH_3); 1.97 (NBu$_4$-*H*); 3.27 (s, 6H, DME-*H*); 3.43 (s, 4H, DME-*H*); 3.81 (NBu$_4$-*H*); 6.28 (d, $^3J_{HH}$ = 6.4 Hz, 4H, Ar-*H*).

Table S1. Crystal data and structure refinement for **2.**

Empirical formula	C54 H74 Fe2 N4 P3	
Formula weight	983.78	
Temperature	150(2) K	
Wavelength	1.54184 Å	
Crystal system	Monoclinic	
Space group	C2/c	
Unit cell dimensions	a = 22.1222(7) Å	α= 90°.
	b = 15.3352(5) Å	β= 92.864(3)°.
	c = 15.7519(5) Å	γ = 90°.
Volume	5337.1(3) Å^3	

Z	4
Density (calculated)	1.224 Mg/m^3
Absorption coefficient	5.489 mm^{-1}
F(000)	2092
Crystal size	0.36 x 0.21 x 0.03 mm^3
Theta range for data collection	3.51 to 67.50°.
Index ranges	-17<=h<=26, -18<=k<=17, -18<=l<=18
Reflections collected	16368
Independent reflections	4826 [R(int) = 0.0837]
Completeness to theta = 67.50°	100.0 %
Absorption correction	Semi-empirical from equivalents
Max. and min. transmission	1.00000 and 0.27522
Refinement method	Full-matrix least-squares on F^2
Data / restraints / parameters	4826 / 0 / 306
Goodness-of-fit on F^2	1.040
Final R indices [I>2sigma(I)]	R1 = 0.0554, wR2 = 0.1489
R indices (all data)	R1 = 0.0595, wR2 = 0.1566
Largest diff. peak and hole	1.063 and -0.531 $e.Å^{-3}$

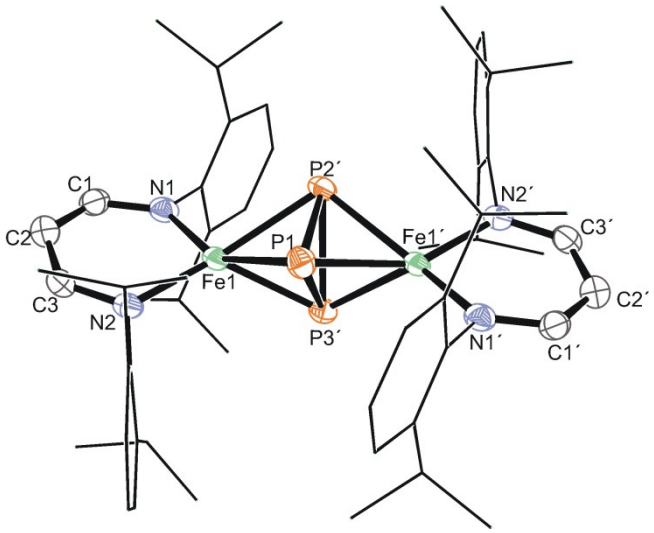

Figure S4. Molecular structure of **2**. The P_3 moiety is equally disordered over two orientations, only one set is depicted. Hydrogen atoms are omitted for clarity. Symmetry transformations used to generate equivalent atoms with (´): -x+1/2,-y+3/2,-z+1.

Table S2. Selected interatomic distances and angles of **2**:

Interatomic distances(Å)	Angles(°)

Fe1-N2	1.951(2)	N2-Fe1-N1	94.18(9)
Fe1-N1	1.962(2)	P2′-P1-P3′	61.35(6)
Fe1-P1	2.339(1)	P1-P2′-P3′	61.83(6)
Fe1-P2′	2.352(1)	P3′-P2′-P1	56.83(5)
Fe1-P3′	2.235(1)		
Fe1′-P1	2.296(1)		
Fe1′-P2′	2.311(1)		
Fe1′-P3′	2.209(1)		
P1-P2′	2.193(2)		
P1-P3′	2.310(2)		
P2′-P3′	2.299(2)		

Table S3. Crystal data and structure refinement for **3**.

Empirical formula	C164 H244 Fe4 K2 N8 O14 P6	
Formula weight	3039.08	
Temperature	150.00(10) K	
Wavelength	1.54178 Å	
Crystal system	monoclinic	
Space group	C 1 2/m 1	
Unit cell dimensions	a = 18.0839(4) Å	α= 90°.
	b = 18.8962(3) Å	β= 115.729(2)°.
	c = 13.6307(2) Å	γ = 90°.
Volume	4196.05(13) Å3	
Z	1	
Density (calculated)	1.203 Mg/m3	
Absorption coefficient	4.162 mm-1	
F(000)	1628	
Crystal size	0.39 x 0.28 x 0.19 mm3	
Theta range for data collection	3.58 to 73.37°.	
Index ranges	-20<=h<=22, -21<=k<=23, -16<=l<=12	
Reflections collected	8670	
Independent reflections	4248 [R(int) = 0.0223]	
Completeness to theta = 73.37°	97.5 %	
Refinement method	Full-matrix least-squares on F2	
Data / restraints / parameters	4248 / 4 / 215	
Goodness-of-fit on F2	1.054	
Final R indices [I>2sigma(I)]	R1 = 0.0757, wR2 = 0.2190	
R indices (all data)	R1 = 0.0828, wR2 = 0.2278	

Largest diff. peak and hole	1.024 and -0.937 e.Å-3

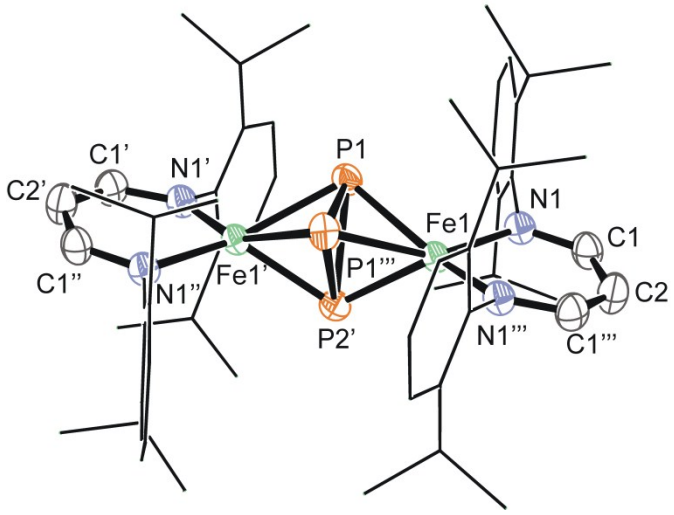

Figure S5. Molecular structure of the anion of **3**. The P_3 moiety is equally disordered over two orientations, only one set is depicted. Hydrogen atoms are omitted for clarity. Symmetry transformations used to generate equivalent atoms with (’’’): x,-y+1,z; (’): -x+1,-y+1,-z; (’’): -x+1,y,-z.

Table S4. Selected interatomic distances and angles of the anion of **3**:

Interatomic distances(Å)		Angles(°)	
P1- P1’’’	2.208(3)	N1-Fe1- N1’’’	92.6(2)
P1- P2’	2.330(3)	P1’’’-P1-P2’	61.72(5)
P2’- P1’’’	2.330(3)	P1’’’-P2’-P1	56.6(1)
Fe1- P1	2.323(2)	P1-P1’’’-P2’	61.72(5)
Fe1- P1’’’	2.323(2)		
Fe1- P2’	2.198(2)		
Fe1’- P1	2.331(2)		
Fe1’- P2’	2.195(2)		
Fe1’- P1’’’	2.331(2)		
Fe1- N1	1.971(3)		
Fe1- N1’’’	1.971(3)		

CV studies on 2

The cyclic voltammogram (CV) of **2** recorded at a scan rate $\nu = 100$ mV·s^{-1} showed a reversible redox

process at $E^{1/2}$ = -1.74 V (*vs* Fc/Fc^+) and several irreversible processes in the anodic region (E^{ox} = -0.68, -0.27, and 0.74 V) as well towards cathodic potentials (E^{red}= -2.24, -2.69, and -3.13 V). The comparison of scans with opposite scan directions indicated that these irreversible electrode processes occur due to oxidative or reductive degeneration, respectively and thus lead to complicated CVs (Fig. S6). We assume, the oxidative irreversibility is due to ligand oxidation considering the redox non-innocence character of β-diketiminate ligands and the reduction irreversibility may have arisen because of distortions in the $[Fe_2P_3]$ core.

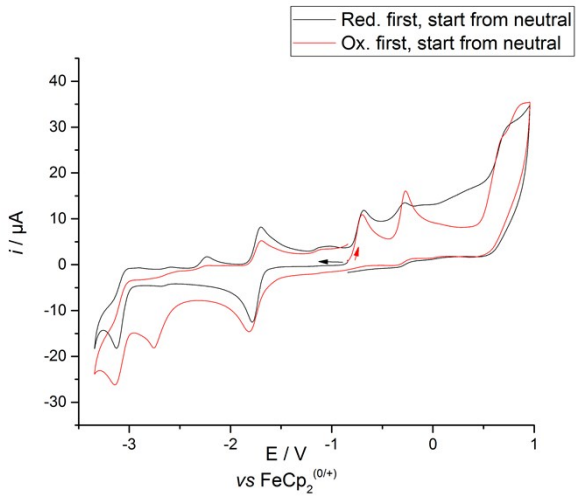

Figure S6. The CV of **2** (1mM in THF/ 0.3M $TBAPF_6$) recorded at a scan rate v = 100 $mV \cdot s^{-1}$.

The redox event at $E^{1/2}$ = -1.74 V (*vs* Fc/Fc^+) was determined to be reversible since the ratio of the peak currents equals 1 for scan rates ν from 50 – 800 $mV \cdot s^{-1}$ (*see* Fig. S7). Slight deviations for other diagnostic criteria (e.g. ΔE_p or $i_{pa}/(v^{1/2})$ vs. ν**)** from perfect reversible behavior are attributed to not fully compensated iR-drop (*see* Tab. S5).

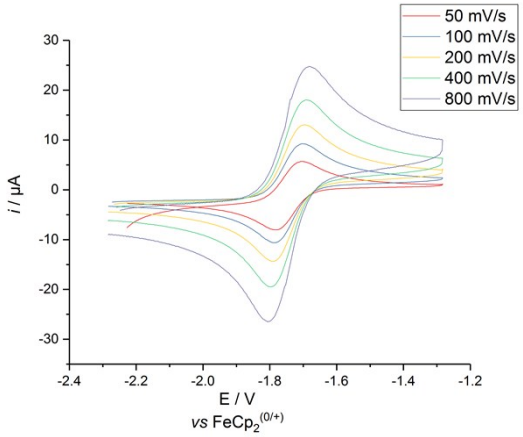

Figure S7. Redox event at $E^{1/2}$ = -1.74 V (*vs* Fc/Fc^+) measured with scan rates v = 50 – 800 $mV \cdot s^{-1}$.

Table S5*: Data for the reversible ET at* $E^{1/2}$ = -1.74 V (*vs* Fc/Fc^+)

v [$mV \cdot s^{-1}$]	E_{pc} [V]	E_{pa} [V]	ΔE_p [mV]	i_{pc} [µA]	i_{pa} [µA]	i_{pa}/i_{pc}	$i_{pa}/(v^{1/2})$

50	-1.779	-1.709	70	7	7	1	0.99
100	-1.785	-1.704	81	10	10	1	1.00
200	-1.788	-1.700	88	13	13	1	0.92
400	-1.786	-1.693	93	17	17	1	0.85
800	-1.802	-1.682	120	22	22	1	0.78

Furthermore, a linear dependence of the forward peak current i_{pa} on the square-root of the scan rate ν implied diffusion control for the redox processes at $E^{1/2}$ = -1.74 V (*vs* Fc/Fc$^+$).

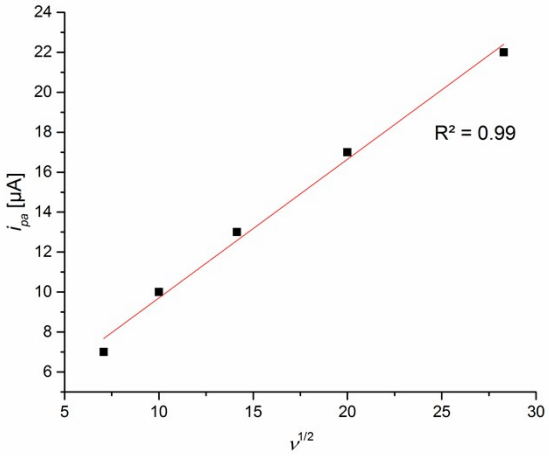

Figure S8. Linear dependence of the forward peak current i_{pa} on the square-root of the scan rate ***v*** indicates diffusion control for the redox process at $E^{1/2}$ = -1.74 V. Linear fits (*red*) were calculated by the least square approach using the model function y = a + bx.

Magnetic Susceptibility Measurement:

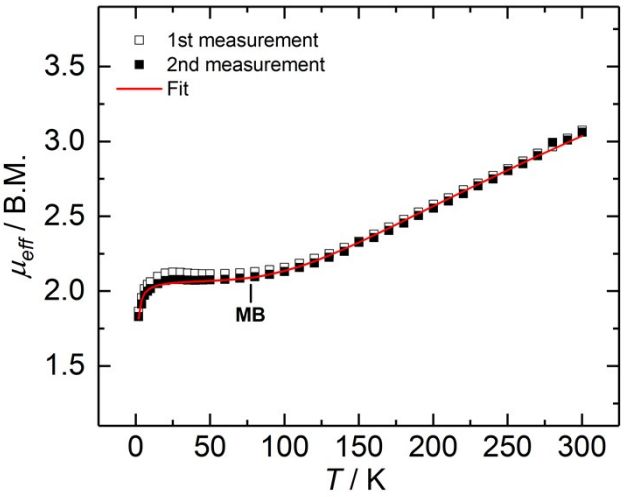

Figure S9. Variable-temperature SQUID magnetization measurement of two independently synthesized batches of **2**, recorded between 2 and 300 K, with an applied magnetic field of 1 T. The graph displays a plot of μ_{eff} vs. temperature for **2**. The red line represents the best fit obtained with parameters of $S_1 = 2.0$, $S_2 = 2.5$, $J_{1,2} = -110$ cm^{-1}, $g_1 = 2.00$, $g_2 = 2.17$, and $\theta_w = -0.52$.

Mössbauer Measurement:

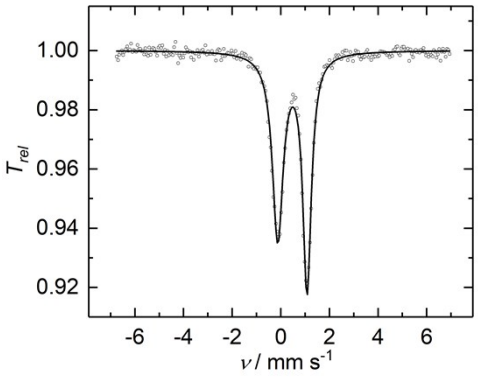

(a)

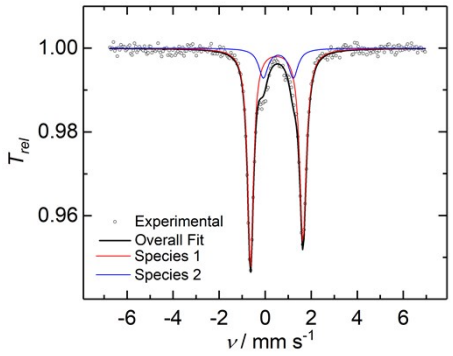

(b)

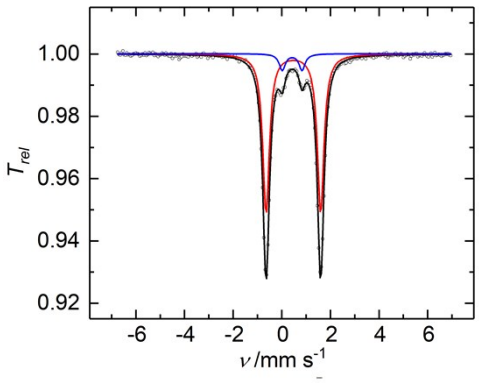

(c)

Figure S10. (a) Zero-field ^{57}Fe Mößbauer spectrum of a microcrystalline sample of **2** (simulated as black line) recorded at 77 K. The solid line (shown in black) represents the best fit obtained with parameters: δ = 0.48(1) mm s^{-1} , ΔE_Q = 1.29(1) mm s^{-1} ($\Gamma_{FWHM,1}$ = 0.53(1) mm s^{-1}, $\Gamma_{FWHM,2}$ = 0.42(1) mm s^{-1}, FWHM = full width at half maximum). The asymmetric doublet was fitted with two quadrupole lines of Lorentzian shape and different linewidths ($\Gamma_{FWHM,1/2}$) but equal integrated area. (b) Zero-field ^{57}Fe Mößbauer spectrum of **3** (simulated as red line) with 18 % of **2** (simulated as blue line) recorded at 77 K. The solid lines are fits with Lorentzian doublets to the experimental values using the following isomer shifts and quadrupole splittings: δ = 0.50(1) mm s^{-1}, ΔE_Q = 2.28(1) mm s^{-1}, Γ_{FWHM} = 0.33 mm s^{-1} for **3**; δ = 0.48(1) mm s^{-1}, ΔE_Q = 1.21(1) mm s^{-1}, Γ_{FWHM} = 0.54 mm s^{-1} for **2**. (c) Zero-field ^{57}Fe Mössbauer spectrum of **4** with 9% unidentified impurity recorded at 77 K. The solid lines are fits with Lorentzian doublets to the experimental spectra using the following isomer shifts and quadrupole splittings: δ = 0.48(1) mm s^{-1}, ΔE_Q = 2.24(1) mm s^{-1} (Γ_{FWHM} = 0.33 mm s^{-1}) for **4**, δ = 0.43(1) mm s^{-1}, ΔE_Q = 0.81(1) mm s^{-1} (Γ_{FWHM} = 0.30 mm s^{-1}) for the unidentified impurity.

EPR spectrum of 2

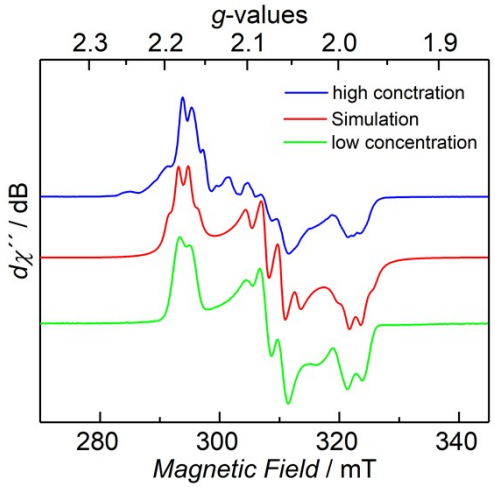

Figure S11. CW X-band EPR spectrum of **2** at 7 K, recorded in frozen toluene solution (black trace), and its simulation (red trace). Experimental conditions: blue line: microwave frequency ν = 8.952 GHz, modulation width = 1.0 mT, microwave power = 1.0 μW, modulation frequency = 100 kHz, time constant = 0.1 s. Green line: microwave frequency ν = 8.951 GHz, modulation width = 1.0 mT, microwave power = 0.01 mW, modulation frequency = 100 kHz, time constant = 0.1 s. Simulation parameters: effective spin $S = 1/2$, effective *g*-values $g_1 = 2.18$, $g_2 = 2.07$, $g_3 = 1.98$, linewidths $W_1 = 0.90$ mT, $W_2 = 0.90$ mT, $W_3 = 0.12$ mT, hyperfine coupling to three equivalent ^{31}P ($I = 1/2$, 100%) nuclei of $A_1 = 51.3$ MHz (1.76 mT), $A_2 = 77.9$ MHz (2.68 mT), $A_3 = 56.4$ MHz (1.94 mT).

C. X-ray absorption spectroscopy and DFT calculations

EXAFS analysis. EXAFS spectra (at 20 K) of the neutral (**2**) and anionic (**3**) diiron compounds with formal $Fe^{III}Fe^{II}$ (**2**) or $Fe^{II}Fe^{II}$ (**3**) valences are shown in Fig. S12. The Fourier-transforms (FTs) of the EXAFS spectra revealed two main peaks due to Fe-N and Fe-P distances, as well as peaks at larger distances due to atoms in the second coordination sphere, as expected (Fig. S12). EXAFS simulations provided the metal-ligand distances in the powder samples (Table S6), which are in good agreement with the crystallographic data, showing that the structures of the compounds in powder material are very similar to the crystal structures. In particular, the Fe-N and Fe-Fe distances, as well as the Fe-P distances differ by less than 0.02 Å on average between both sample types. Two different Fe-P distances (1x ~2.19 Å and 2x ~2.32 Å) could be resolved in the EXAFS data, similar to the crystal structures, and a slight elongation (mean of ~0.03 Å) of the Fe-N bonds in **3** vs **2** was apparent in the EXAFS and crystal data. In both the EXAFS and crystal data, the Fe-Fe distance was significantly (~0.05 Å) elongated in the more reduced **3**. These results reveal that complex reduction had occurred in **3**, but causes relatively minor effect on the global structure in powder and crystalline materials of both compounds.

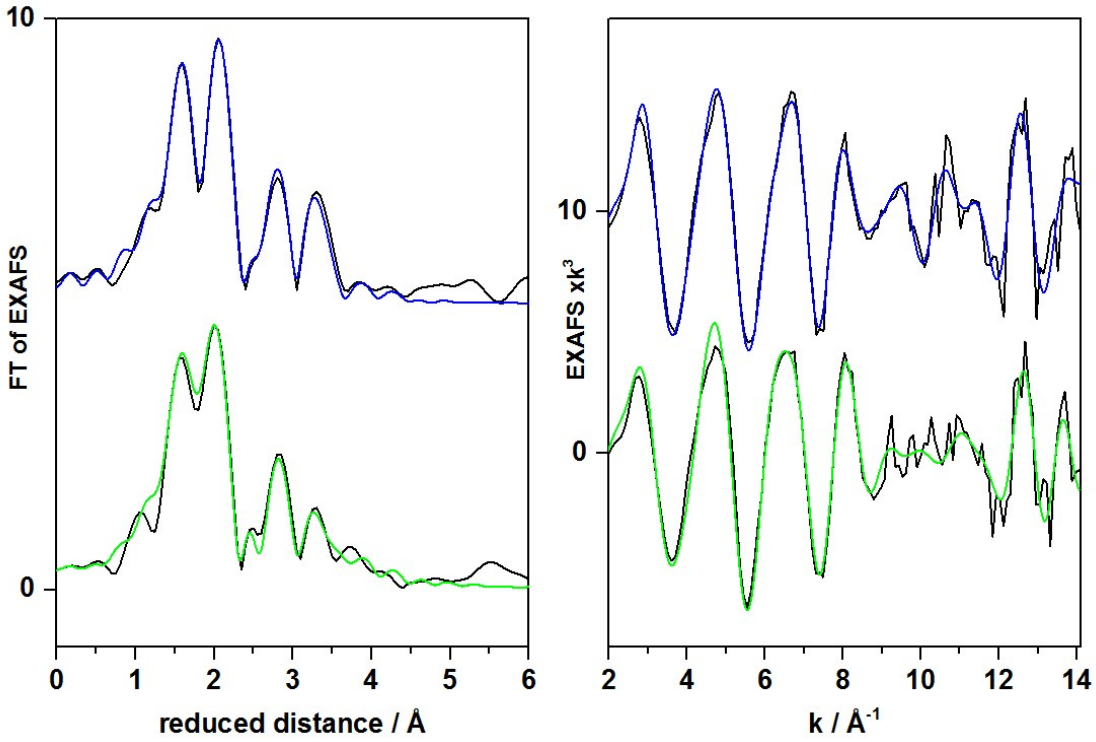

Figure S12: EXAFS spectra of diiron compounds. Data of the neutral (**2**, top) and anionic (**3,** green) compounds are compared (spectra were vertically shifted; left panel, Fourier-transforms of the EXAFS oscillations in the right panel; black lines, experimental data; colored lines, simulations with parameters in Table S6).

Table S6: EXAFS fit parameters.[a]

	2 ($Fe^{III}Fe^{II}$)			**3** ($Fe^{II}Fe^{II}$)		
shell	N [per Fe]	R [Å]	$2\sigma^2 x10^3$ [$Å^2$]	N [per Fe]	R [Å]	$2\sigma^2 x10^3$ [$Å^2$]
Fe-N	2*	1.94 (1.95)	5	2*	1.97 (1.97)	4
Fe-P	1*	2.20 (2.23)	2#	1*	2.18 (2.20)	2#
Fe-P	2*	2.32 (2.34)	3	2*	2.32 (2.32)	5
Fe-Fe	1*	3.72 (3.75)	2#	1*	3.67 (3.70)	2#
Fe-C	3*	2.94 (2.93)	2#	2*	2.96 (2.96)	2#
Fe-C	2*	3.22 (3.10)	2#	3*	3.23 (3.08)	2#
Fe-C	4*	3.89 (3.79)	2#	4*	3.88 (3.79)	2#

[a]N, coordination number; R, interatomic distance; $2\sigma^2$, Debye-Waller factor; the fit error sum, R_f, was calculated for reduced distances of 1.0-3.5 Å and was 7.3 % for **2** and 14.1 % for **3**. *Coordination numbers that were fixed in the fits to the crystallographic values, #$2\sigma^2$ fixed to physically reasonable values. Distances in parenthesis refer to crystal structures.

XANES spectra. Fe K-edge spectra of **2** and **3** are compared to spectra of previously studied, related diiron compounds[1] containing formal Fe(II) or Fe(III) ions in Fig. S13 (K-edge energies are given in the legend). Differences in the spectral shapes of **2** and **3** are well discernable, reflecting the subtle geometry changes at the metal centers upon reduction as revealed by crystallography and EXAFS. The K-edge energy of **3** was similar to the one of a (formal) Fe(II) reference compound (**2** in ref.[8]). The K-edge energy of **3** was only slightly (~0.1 eV) lower vs. **2** and the energy of **2** was well below the one of (formal) Fe(III)Fe(II) and Fe(III)Fe(III) compounds (**3** and **5** in ref.[8]). The mean iron oxidation level in **2** thus was close to Fe(II), meaning that few apparent oxidation of the metal centers occurred in **2** and electron density may be extracted mostly from the ligands. The pre-edge feature in the XANES (around 7113 eV, see Fig. S13) reflects formally dipole-forbidden excitation of a core level (1s) electron into unoccupied valence levels with mostly Fe(d) character. The single pre-edge feature of **2** was peaking at ~0.5 eV higher energy and its amplitude was slightly increased compared to **3** (Fig. S14). This observation suggests changes in the configuration of unoccupied valence levels in the two compounds. The electronic transitions underlying the pre-edge absorption and the electronic structures of the compounds in the low-spin states (as realized at 20 K) are analyzed using DFT calculations in the following.

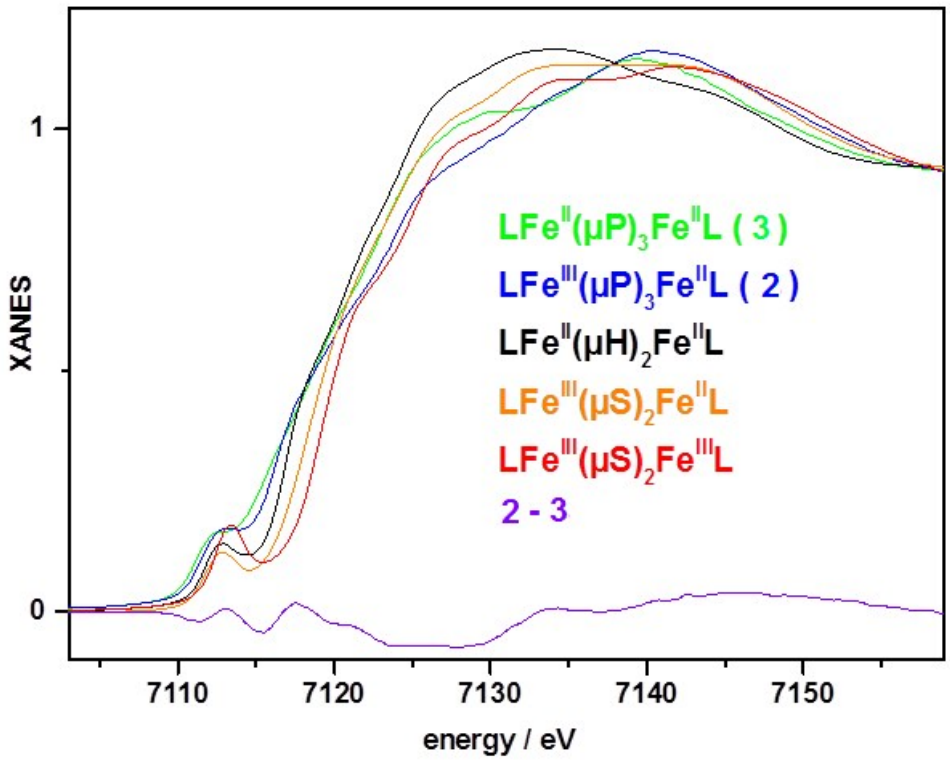

Figure S13: XANES spectra of diiron compounds. Spectra of compounds **3** and **2** are compared to spectra of previously studied, related compounds (complexes **2**, **5**, and **3** in ref.[8] , L = ligands, given iron oxidation states refer to formal valences) and **2** – **3** difference spectrum. K-edge energies are (at 0.5 level) as follows: **3**, 7118.7 eV; **2**, 7118.8 eV; **2^{r}**, 7118.6 eV; **5^{r}**, 7119.4 eV; **3^{r}**, 7120.1 eV.

Quantum chemical calculations. Due to disorder in the crystal structures of **2** and **3**, which simulate a center of inversion within the central P_3 moiety, possible differences in the local coordination environment of the formal Fe(III) and Fe(II) ions may be hidden in the atomic displacement parameters. The disorder is not vanishing when the structure is refined in related space groups without a center of inversion such as C2 or Cc, meaning that bond lengths differences between the two iron ions remain invisible. A certain conclusion from the crystal data is that the Fe-Fe distance is ~0.05 Å longer in **2**, despite the higher mean formal oxidation state (+2.5 in **2** vs. +2 in **3**), and that there are one shorter Fe-P distance (~2.2 Å) and two longer Fe-P distances (~2.3 Å), resulting in a P_{1+2} rather than a P_3 ligation pattern, in agreement with the EXAFS analysis. Subtle differences between the bond lengths at the two iron ions in **2** and **3** are revealed though in geometry-optimized structures from DFT, including anti-ferromagnetically coupled high-spin formal Fe(III/II) species (Table S7).

Table S7: Bond lengths of **2** and **3** in geometry-optimized structures from DFT.[a]

	2	**3**	**3 – 2**
	R [Å]		ΔR [Å]
Fe1-Fe2	3.90 (3.72)	3.86 (3.67)	-0.04 (-0.05)
Fe1-N	1.99	1.98	-0.01
Fe1-P1	2.29	2.27	-0.02
Fe1-P2/3	2.44	2.39	-0.05
Fe2-N	1.96	1.98	0.02
Fe2-P1	2.26	2.27	0.01
Fe2-P2/3	2.35	2.38	0.03
$Fe\text{-}N_{mean}$	1.98 (1.94)	1.99 (1.97)	0.01 (0.03)
$Fe\text{-}P1_{mean}$	2.28 (2.20)	2.27 (2.18)	-0.01 (-0.02)
$Fe\text{-}P2/3_{mean}$	2.40 (2.32)	2.39 (2.32)	-0.01 (0.00)
	ΔR(Fe1-Fe2)		ΔΔR(Fe1-Fe2)
Fe-N	-0.03	0.00	0.03
Fe-P1	-0.03	0.01	0.04
Fe-P2/3	-0.09	-0.01	0.08

[a]Bond lengths and differences from EXAFS are given in parenthesis, "mean" denotes average values over both iron ions referred to as 1 and 2 (Fe^{III}/Fe^{II} in **2** and Fe^{II}/Fe^{II} in **3**).

Metal-ligand bond lengths from DFT were slightly overestimated compared to the crystal and EXAFS data (Table S7), which is typical for the used theory level. Otherwise, the Fe-P/N and Fe-Fe distances, as well as the mean distance differences between **2** and **3** from DFT closely reproduced the experimental trends, in particular featuring slight Fe-N bond shortening in **2**, but Fe-P bond and Fe-Fe distance elongation in the more oxidized compound (**2**). These changes suggest a significant redistribution of electron density upon reduction of **2** to form **3**. The DFT structures further revealed significant asymmetry of the two metal sites in particular in **2**, with Fe-N/P bond lengths being shorter or longer by up to ~0.1 Å at one iron site vs. the other iron site. This suggests considerable localization of the valence electrons.

The electronic situation in **2** and **3** was verified by comparing experimental and calculated pre-edge absorption features (Fig. S14). The small pre-edge amplitude of **2** and **3** (i.e. in comparison to reference compounds, see Fig. S13) suggests diminished ligand(p)-metal(d) orbital mixing, which presumably is due to the unusual coordination geometry. For **2**, this may be considered as a combination of a tetrahedrally distorted trigonal-planar $N_2\text{-}Fe^{III}$-P(1) coordination (C_L-Fe-P(1) angle = 164°; C_L = central C atom of L) with a pyramidal distorted square-planar $N_2\text{-}Fe^{II}$-P(2,3) coordination (P(2/3)-Fe-N(1/2) trans angle = 152°). The shape and energy changes of the experimental pre-edge spectra are well

reproduced by the spectra from TDDFT (Fig. S14), meaning that the theoretical electronic structures adequately model the situation in the compounds at low temperature (20 K). The electronic transitions in the pre-edge region can be characterized by the difference electron density of ground state and individual excited states (Fig. S15). The transitions at lowest energies involve the LUMOs, which are localized at one iron center in **2** and **3** and show Fe-d(z^2) (Fe1) or Fe-d(x^2-y^2) (Fe2) characters in **2** and Fe-d(x^2-y^2) characters (Fe1 and Fe2) in **3**. Transitions for increasingly higher energies show the excited electron mostly in orbitals with Fe(d) character and increasing delocalization over both metal ions, as well as increasing delocalization onto the terminal ligands in particular for **3**. For **3**, both iron ions show practically identical contributions to the pre-edge. For **2**, the two iron ions show significantly different contributions, with Fe1, corresponding to the formal Fe(III) center, mostly accounting for the pre-edge spectral differences between **2** and **3**, such as increased/decreased intensities at lowest/highest pre-edge energies (7113/7115 eV) and the pronounced shoulder at low energies (7118 eV) in the main-edge rise. Accordingly, for **3** charge-transfer transitions onto the ligands are more prominent, whereas the pre-edge of **2** is dominated by excitation into metal-centered orbitals, indicating a lower degree of electron delocalization in **2**.

An estimate of the degree of anti-ferromagnetic coupling (afc) is provided by the diradical character of the broken-symmetry wavefunction from TDDFT. It can be quantified and visualized with unrestricted Hartree-Fock corresponding orbitals (UCOs), which are extracted from the canonical orbitals by unitary transformations to result in maximal overlap between α and β orbitals.[17] Orbitals with an overlap integral >0 and <1 account for afc (Fig. S16, Table S8). For **2**/**3**, four/five such UCOs are obtained, one/two with strong overlap (>98 %), two with medium overlap (50-75 %), and one with low overlap (<8 %), resulting in increasing diradical characters of 0.02 to 1.00. Expectedly, UCOs oriented towards the central P_3 fragment show stronger overlap. Moreover, **2** has one UCO of 0 % overlap (Fe-d(z^2) character), representing the unpaired electron of the Fe(III) site. Taking all five UCOs into account, a higher diradical character is obtained for the mixed-valence state in **2** (0.66 compared to 0.45 in **3**), despite similar afc behavior of the coupling electrons. Complementary to the orbital picture, the unpaired electrons can be analyzed in real-space by means of the spin-density (SD) (Fig. S17, Table S9).[25] The iso-surface representation uncovers a considerable α-SD distribution over P(1) and a smaller distribution also over the adjacent N and remaining P atoms. The β-SD reflects the pronounced spin polarization as a consequence of the afc. The atomic and fragmental CM5 charges[5] (Table S9) show that the surplus electron in **3** mainly resides on the terminal ligands (~0.30 each) and the P_3 moiety (~0.25) and only a small amount of charge (~0.15) is shared between the two equally charged iron sites. The one-electron oxidation in **2** results in a significant redistribution of charges over the iron sites, with Fe1(III) gaining charge and Fe2(II) loosing charge ($\Delta Q_{Fe1-Fe2} = 0.5$), resulting in a similar summed charge on iron as in **3**

(as supported by the K-edge energies), but further emphasizing the pronounced asymmetry of the two iron sites in **2**.

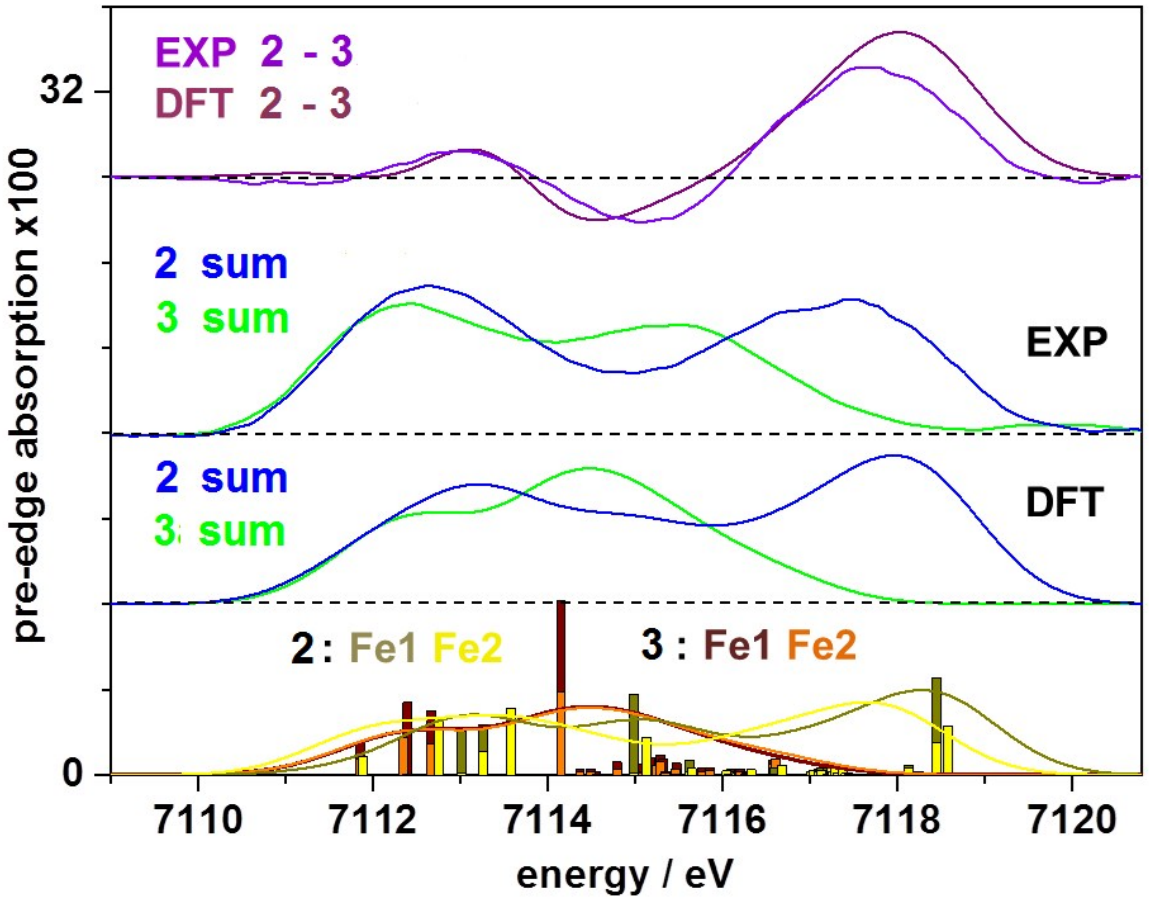

Figure S14: Pre-edge absorption features from experiment and theory. Difference spectra (**2** – **3**) are compared to experimental (EXP) and calculated (TDDFT) sum spectra of the contributions of the individual iron ions (Fe1 and Fe2) in **2** and **3**. Spectra are vertically shifted for clarity. Stick spectra (x3) of Fe1 and Fe2 are shown for comparison. Experimental spectra in the pre-edge and low-energy edge region were extracted from the XANES spectra (Fig. S13) by subtraction of the same smooth (polynomial) main-edge rise background from the **3** and **2** spectra. Stick spectra (40 sticks in a 7111.8-7118.6 eV range) from TDDFT were broadened by Gaussians (FWHM 1.5 eV) to derive line spectra. The calculated energy axis was multiplied by a factor of 1.15 and spectra were shifted afterwards by -1067.2 eV and scaled by a factor of 200 for alignment with experimental data.

Table S8: Diradical character[a] of corresponding orbital pairs.

3			**2**		
orbital. no.	overlap integral	diradical character, D [%]	orbital no.	overlap integral	diradical character, D [%]
257	0.990	0.02	257	0.981	0.04
258	0.986	0.03	258	0.654	0.57
259	0.742	0.45	259	0.551	0.70
260	0.497	0.75	260	0.057	1.00
261	0.071	0.99	261	0.000	1.00
total		0.45	total		0.66

[a]The diradical character is calculated from the overlap integrals (x) by: $D = 1 - x^2$.[17]

Table S9: Spin densities and atomic/fragmental charges.

	2		**3**	**2 – 3**
	MSD[a]	Q_{CM5}[b]	Q_{CM5}[b]	ΔQ_{CM5}[b]
$Fe1^{III/II}$	3.10	0.60	0.27	0.33
$Fe2^{II}$	-2.31	0.10	0.27	-0.17
P_3	0.13	-0.21	-0.45	0.24
L(Fe1)	0.06	-0.26	-0.54	0.28
L(Fe2)	0.02	-0.24	-0.54	0.26
sum	1.00	0.00	-1.00	-1.00

[a]MSD = Mulliken spin densities, [b]Q_{CM5} = variant of Hirshfeld charges, L = terminal ligands.

Mayer bond orders (MBO)[16] were calculated (Table S10). The MBOs indicate a weak through-space Fe-Fe interaction in **2** (0.27) and **3** (0.24). An MBO close to unity is obtained for the P(2)-P(3) bond connecting the symmetry-equivalent P atoms, whereas considerably lower MBOs are obtained for the slightly longer P(1)-P(2,3) bonds. Because the surplus electron in **3** is distributed over the molecule, only negligible MBO differences in both complexes are found for the P_3 moiety. The Fe-P bonds, although longer than the Fe-N bonds, show larger MBO values, which is due to low electron sharing in the strongly polar Fe-N bonds. These trends are supported by topological bond descriptors derived from atoms-in-molecules (AIM) theory[26] (Fig. S18, Table S10). AIM provides bond path motifs, which uncover numerous weak H···P, H···H, and π···π contacts. All P-P, Fe-P, and Fe-N bonds fall into the regime of polar-covalent interactions with electron density (ρ) values at the so-called bond critical points (bcp) roughly between 0.5 and 1.0 Å, a Laplacian of the electron density ($\nabla^2\rho$) being positive, but typically close to zero, and kinetic (G/ρ) energy density over electron density ratios being positive and total (H/ρ) energy density over electron density ratios being negative. Large positive G/ρ values are associated with a high

degree of bond polarization, large negative H/ρ values are associated with a high degree of covalency. In this sense, the P-P bonds are most covalent, showing large ρ values, an already slightly negative $\nabla^2\rho$, the smallest positive G/ρ, and the highest negative H/ρ values. The Fe-N bonds are least covalent, showing medium ρ values, strongly positive $\nabla^2\rho$, and by far the most positive G/ρ and least negative H/ρ values. The Fe-P bonds show intermediate properties.

Table S10: Mayer bond orders and bond topological properties.

	bond	d_1+d_2 [Å]	MBO[a]	ρ_{bcp} [eÅ^{-3}]	$\nabla^2\rho_{bcp}$ [eÅ^{-5}]	ε	G/ρ_{bcp} [a.u.]	H/ρ_{bcp} [a.u.]
2	Fe2^{II}-P1	2.260	0.78	0.57	2.2	0.19	0.68	-0.41
3	Fe1,2^{II}-P1	2.266	0.77	0.57	2.2	0.10	0.67	-0.41
2	Fe1^{III}-P1	2.293	0.79	0.56	1.6	0.11	0.59	-0.40
2	Fe2^{II}-P2/3	2.351	0.66	0.49	2.1	0.48	0.65	-0.35
3	Fe1,2^{II}-P2/3	2.390	0.62	0.45	2.3	0.53	0.68	-0.33
2	Fe1^{III}-P2/3	2.440	0.56	0.42	1.8	0.13	0.60	-0.30
2	P2-P3	2.199	0.93	0.73	-2.1	0.23	0.34	-0.54
3	P2-P3	2.199	0.95	0.72	-2.0	0.27	0.34	-0.53
2	P1-P2/3	2.309	0.76	0.60	-0.6	0.33	0.37	-0.44
3	P1-P2/3	2.334	0.74	0.57	-0.3	0.41	0.38	-0.41
2	Fe2^{II}-N	1.961	0.63	0.66	10.2	0.12	1.33	-0.24
3	Fe1,2^{II}-N	1.977	0.61	0.62	10.3	0.12	1.39	-0.22
2	Fe1^{III}-N	1.995	0.66	0.62	9.0	0.38	1.25	-0.24

[a]MBO = Mayer bond order, [b]topological bond properties from electron density analysis according to the atoms-in-molecules (AIM) theory. For parameter descriptions see the text.

A characteristic and unifying feature of the P-P, Fe-P, and Fe-N bonds in **2** and **3** is the high bond ellipticity (ε) of 0.1-0.5, which indicates "electron smearing" in terms of asymmetric electron density distribution perpendicular to the bond axis, in contrast to localized bonds, for which values below 0.05 are expected. This finding is supported by the formation of a cage-shaped non-covalent interactions indicator (NCI)[27] basin, which encloses the complete FeP_3Fe part (Fig. S19). NCI calculates the reduced electron density gradient ($s = [1/2(3\pi^2)^{1/3}]|\nabla\rho|/\rho^{4/3}$) and NCI iso-surfaces were chosen in a way to display exclusively non-covalent interactions, including steric H···H contacts, hydrogen bonds, and non-covalent bonding aspects of polarized covalent metal-ligand bonds. MBO, AIM, and NCI analyses clearly favor an asymmetric P_{1+2} ligation model over a P_3 ligation model in **2** and **3**.

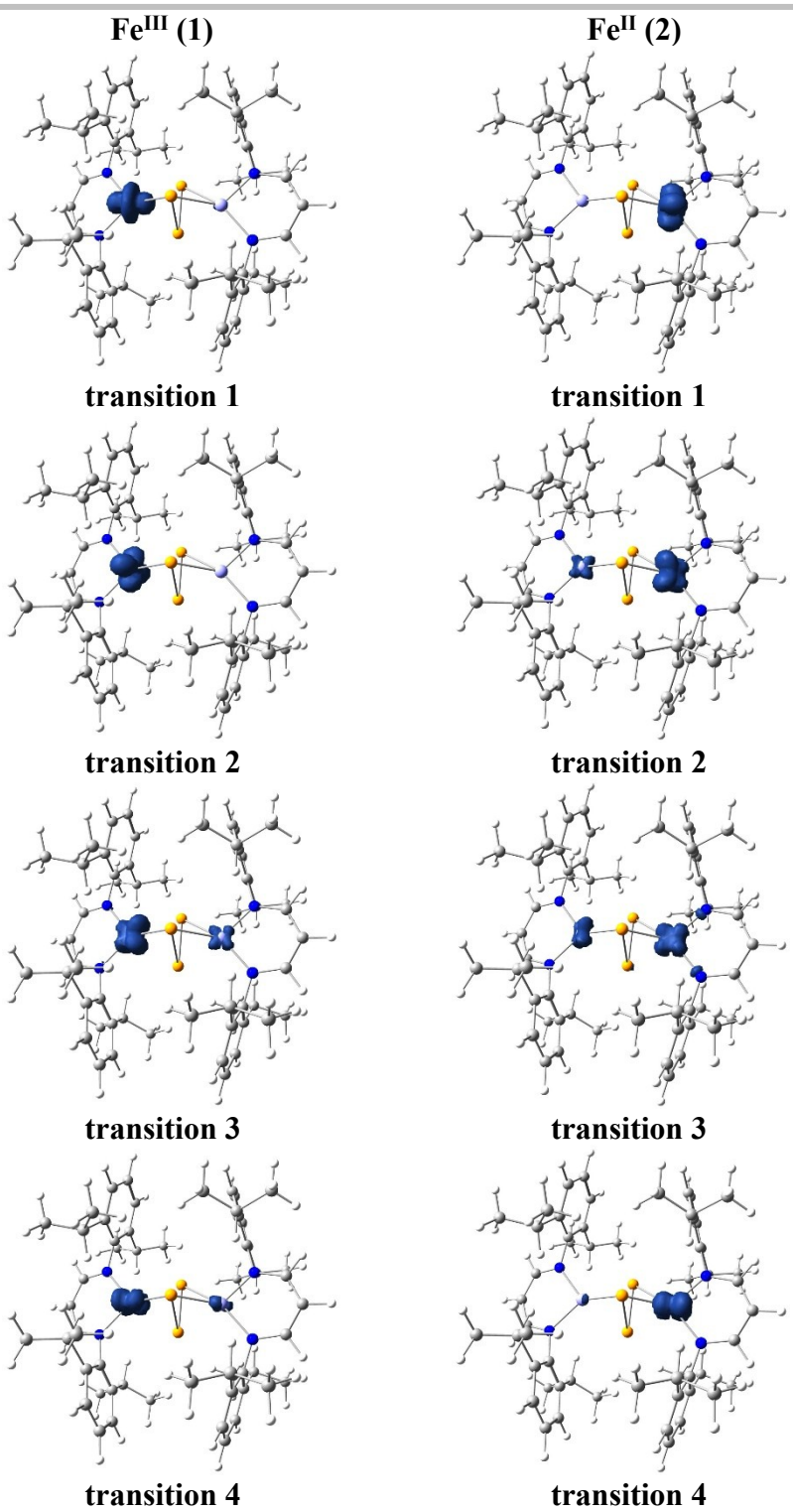

Figure S15A: Electronic transitions underlying the pre-edge absorption. Shown are difference electron densities (at 0.01 iso-surface) for Fe1 (left) and Fe2 (right) between individual excited state and electronic ground state in **2**, which account for electronic transitions in the X-ray pre-edge absorption region. Transition numbers refer to increasing energies (Fig. S14).

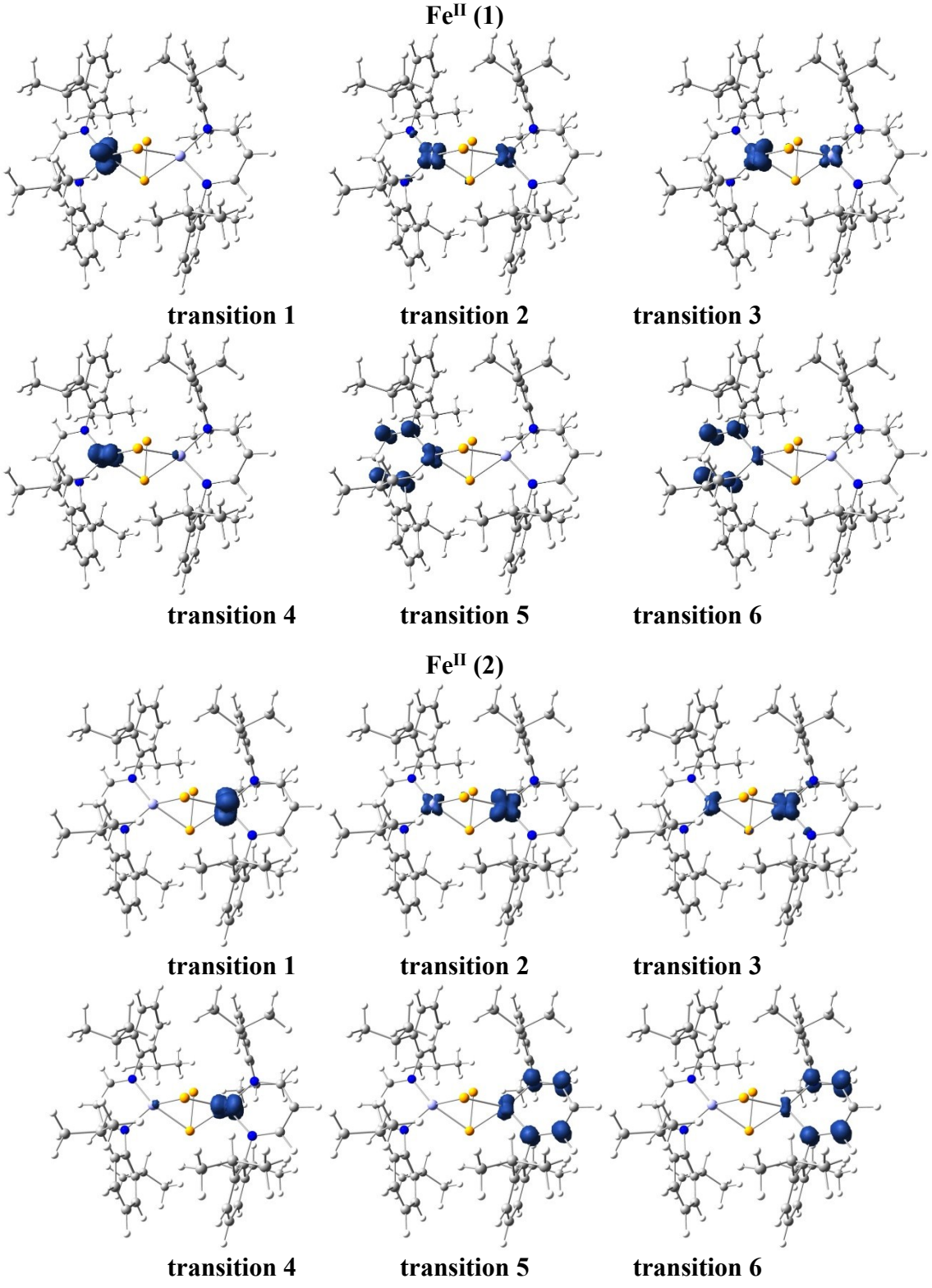

Figure S15B: Electronic transitions underlying the pre-edge absorption. Shown are difference electron densities (at 0.01 iso-surface) for Fe1 (top) and Fe2 (bottom) between individual excited state and electronic ground state in **3**, which account for electronic transitions in the X-ray pre-edge absorption region. Transition numbers refer to increasing energies (Fig. S14).

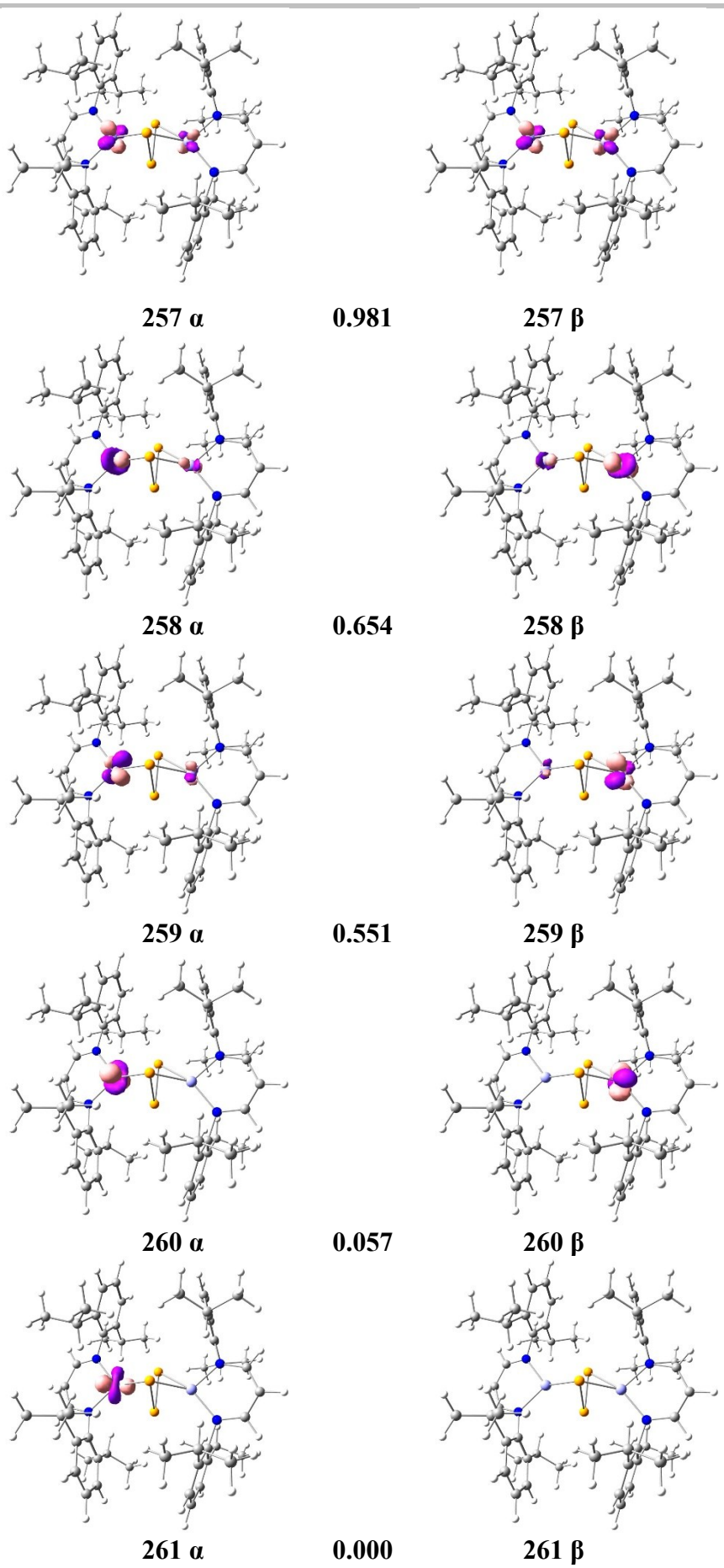

Figure S16A: Corresponding MOs (at ±0.1 iso-surface) of **2** and overlap integrals (in %).

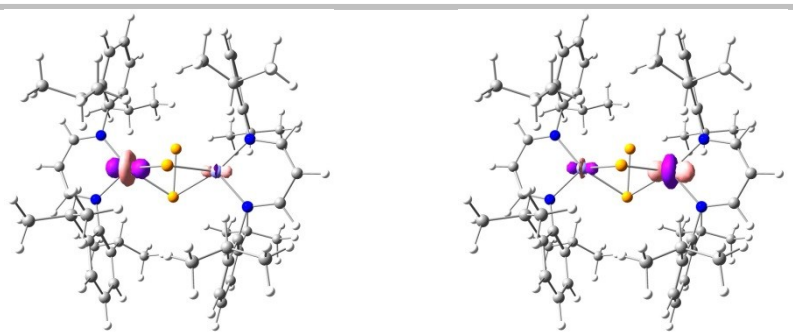

257 α **0.990** **257 β**

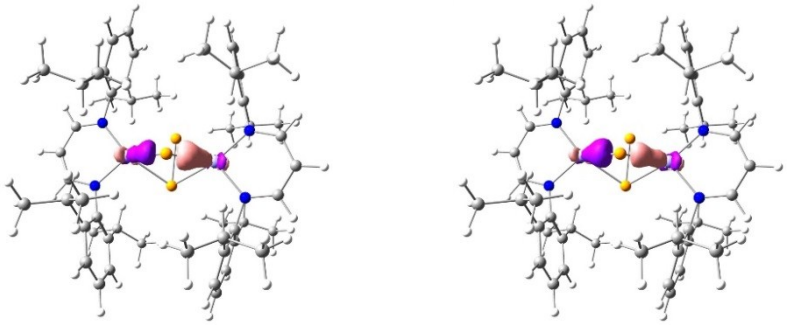

258 α **0.986** **258 β**

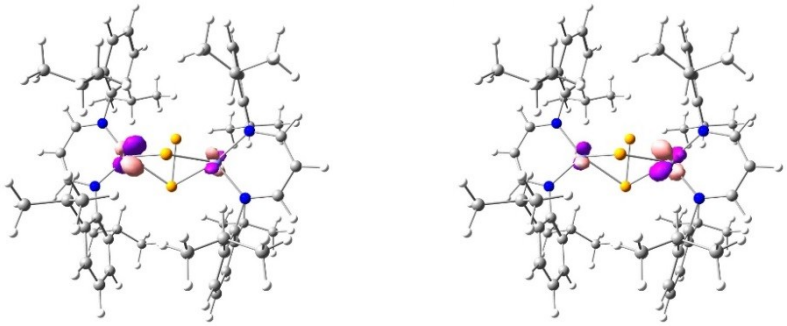

259 α **0.742** **259 β**

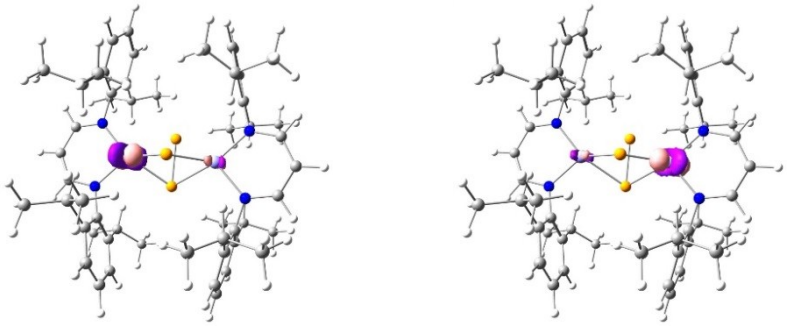

260 α **0.497** **260 β**

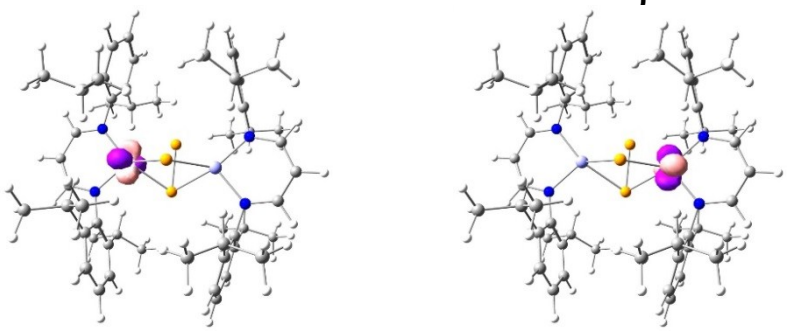

261 α **0.071** **261 β**

Figure S16B: Corresponding MOs (at ±0.1 iso-surface) of **3** and overlap integrals (in %).

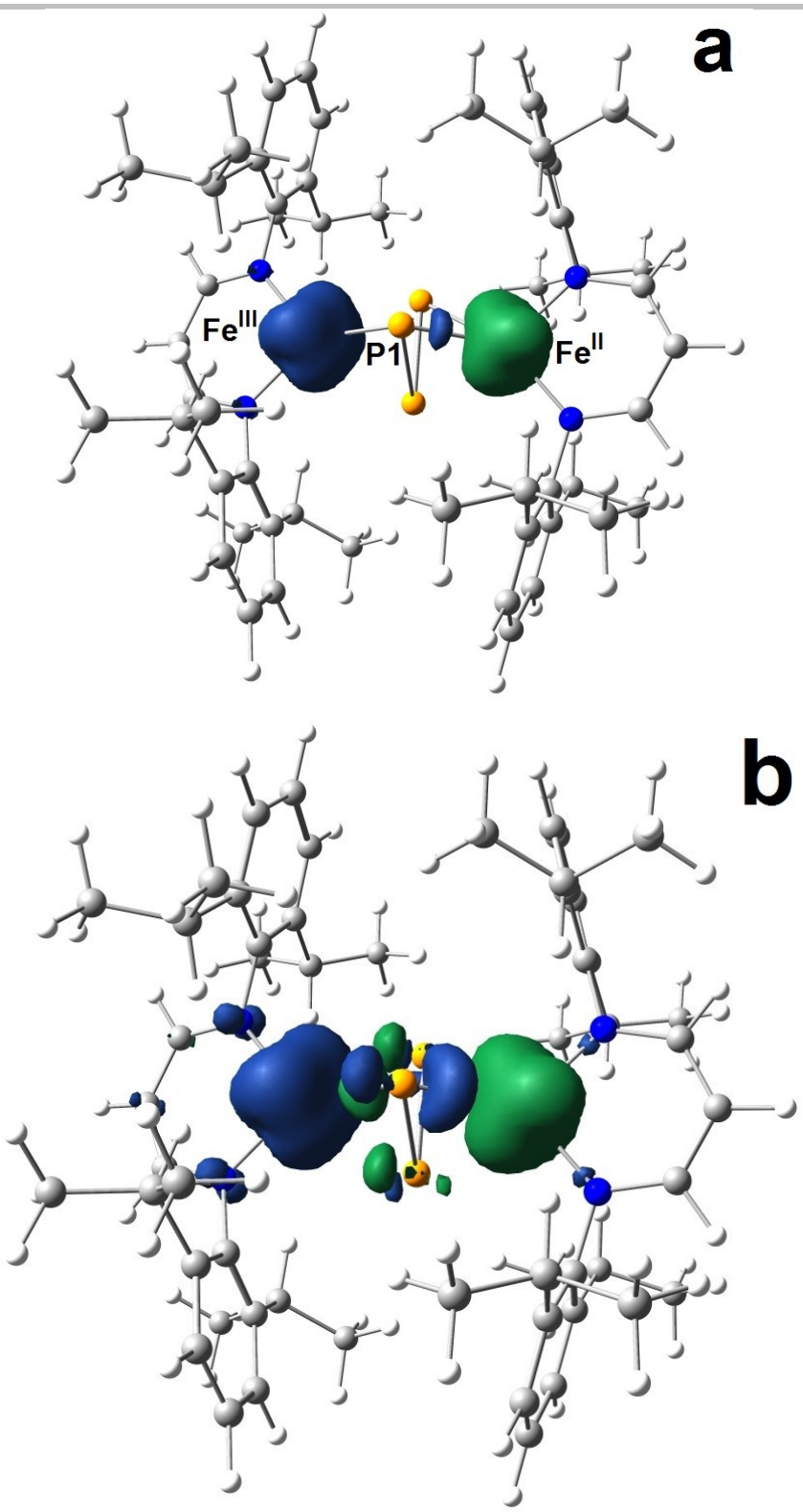

Figure S17: Spin density distribution in **2**. SDs are displayed at two different iso-values (a, ±0.010; b, ±0.005; α-SD in blue and β-SD in green). The prominent role of the special μP atom (labeled P1) in carrying significant spin density is apparent.

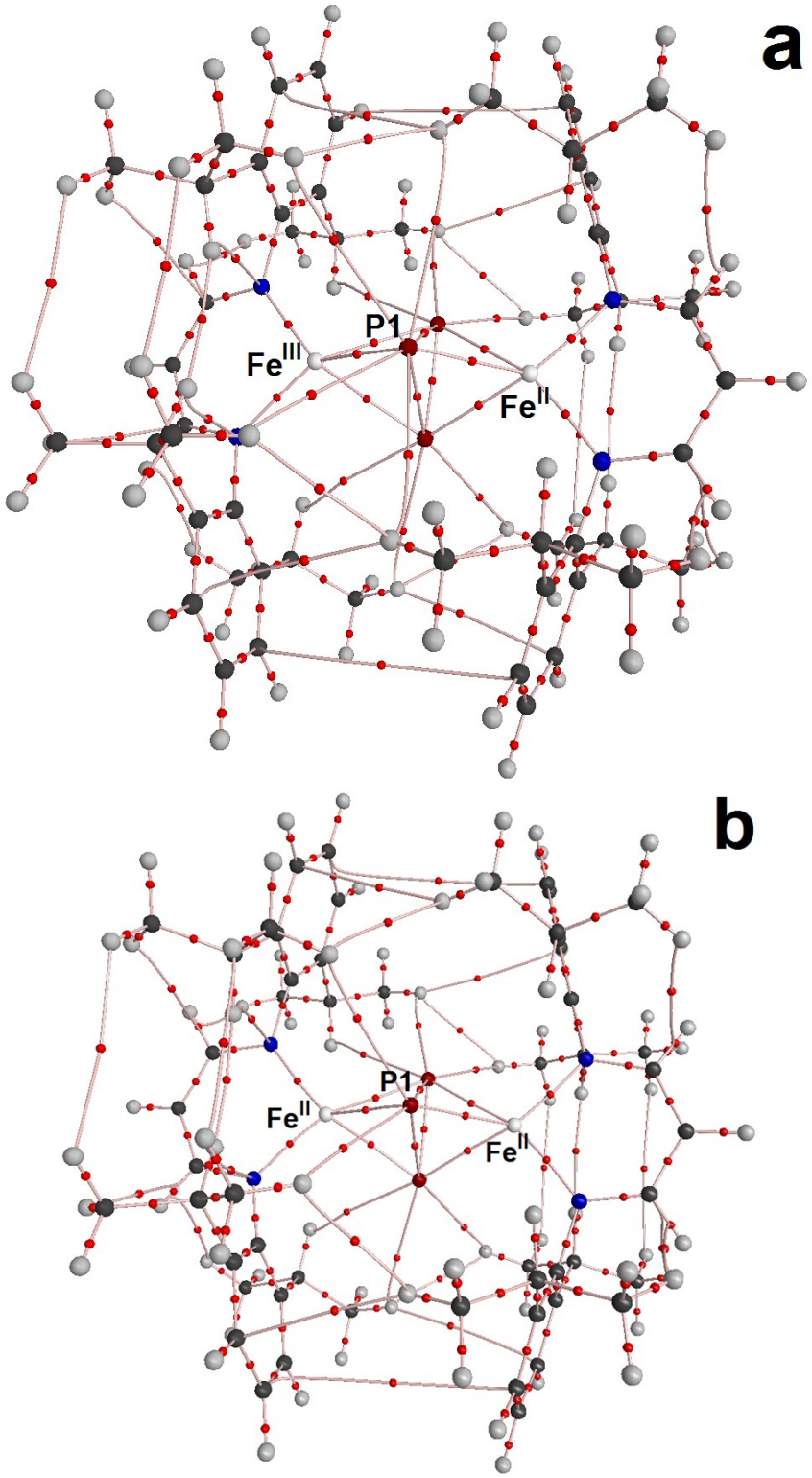

Figure S18: AIM bond topologies in **2** (a) and **3** (b). The special P atom is labeled P1. Bond critical points (red dots) connect the P_{2+1} fragment with the iron atoms. Both structures are stabilized by numerous weak H···H, H···P, and π···π interactions.

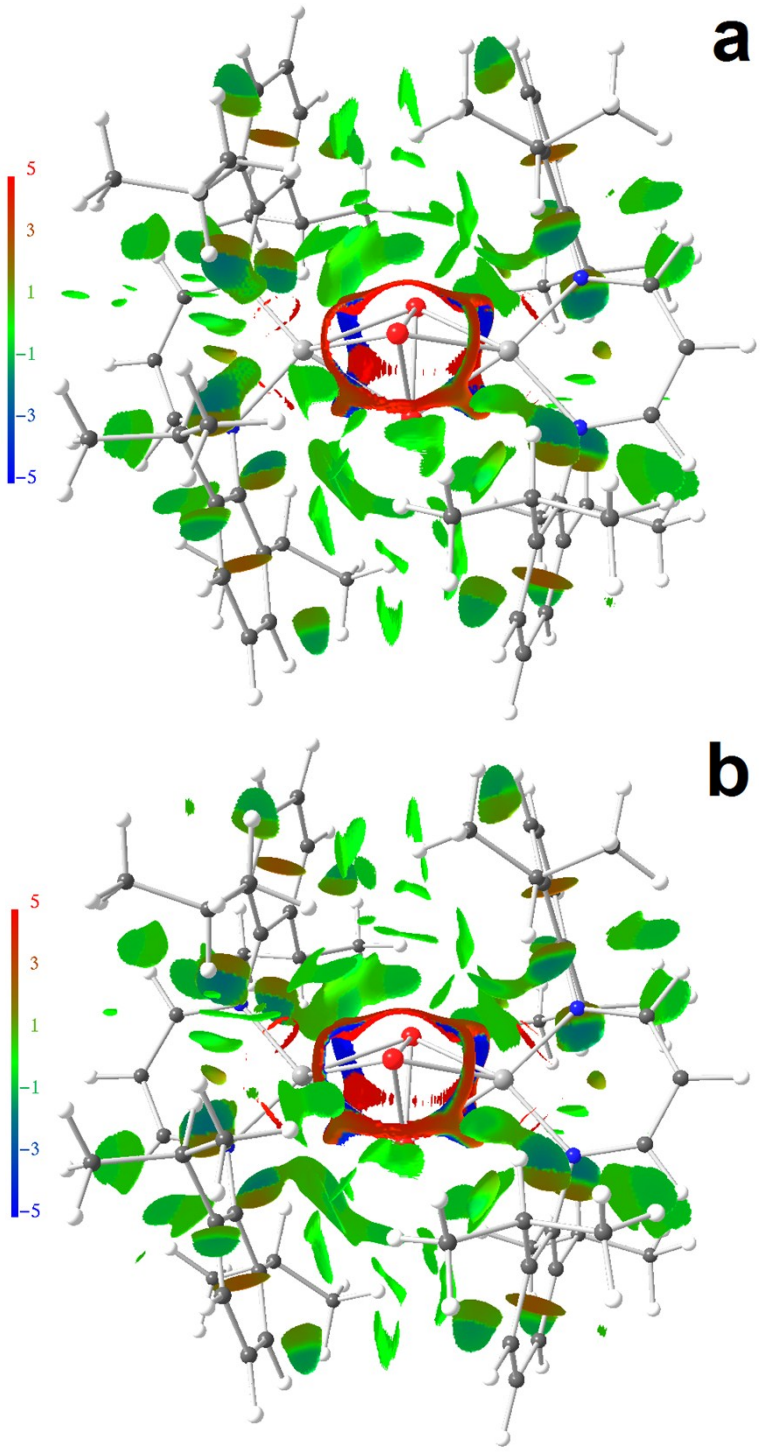

Figure S19: Non-covalent interactions indicator iso-surfaces for **2** (a) and **3** (b). NCIs are shown at **s** = 0.5 level. The red/blue colored NCI basin, which encloses the central P_3 fragment, indicates pronounced electron delocalization in this region. The flat green-colored basins represent weak H···H, H···P, and π···π interactions. The electron density multiplied by the sign of the second eigenvalue of the Hessian ($sign(\lambda_2)\rho$) as mapped on the iso-surfaces facilitates attribution of contact types to steric/repulsive, Van-der-Waals like, or attractive interactions ($\lambda_2 > 0$, $\lambda_2 \approx 0$, or $\lambda_2 < 0$; red, green, or blue colors).

D. Material Synthesis, Characterization and Reactivity Measurements

Synthesis of FeP electrocatalyst

First, 20 ml of oleylamine was placed in a three-necked round bottom Schlenk flask fitted with a temperature sensor and a condenser. The whole set up was degassed using vacuum and refilled with nitrogen twice. Subsequently, the flask was heated to 300 °C. Complex **2** (0.25 g) in 5 mL of dry oleylamine was placed in a second flask which was then transferred to the three-necked flask at 300 °C under inert conditions. The reaction temperature was maintained at 300 °C for one more hour, the heating was removed and the mixture was allowed to cool down to room temperature. Finally, the reaction mixture was transferred into a centrifuge tube by the addition of 20 mL acetone and centrifuged at 9000 rpm to produce a black precipitate, which was then thoroughly washed several times to remove any excess ligand and oleylamine. The black precipitate (20 mg, yield 90% with respect to Fe and net carbon content was 6% as per C, H, N analysis) was dried and stored for further characterisation. Since the free ligand is not stable at 300 °C, we assume that the released free ligand from the Fe_2P_3 cluster after hot injection may have converted in to unidentified smaller organic fragments and got separated from the FeP nanoparticles during the washing process.

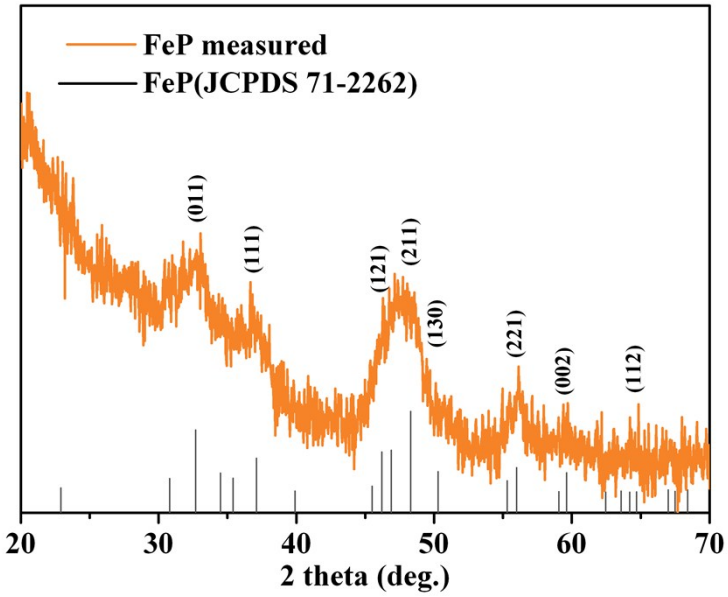

Figure S20. PXRD of FeP with intense Miller indices (hkl) indices synthesized via the hot-injection approach (JCPDS 71- 2262).[28] The obtained FeP material had very small crystallites (see TEM later on) resulting in the very weak diffraction pattern. The phase confirmation was additionally carried out using TEM, HRTEM, EDX, ICP-AES and XPS analysis.

Table S11: Determination of iron and phosphorous ratio in FeP was obtained by EDX, ICP-AES and XPS analysis. Three independent measurements were performed for the reliability and the average data is presented.

	Theoretical	EDX	ICP-AES	XPS
FeP	**1:1**	~1:0.97	1:1.01	~1:1

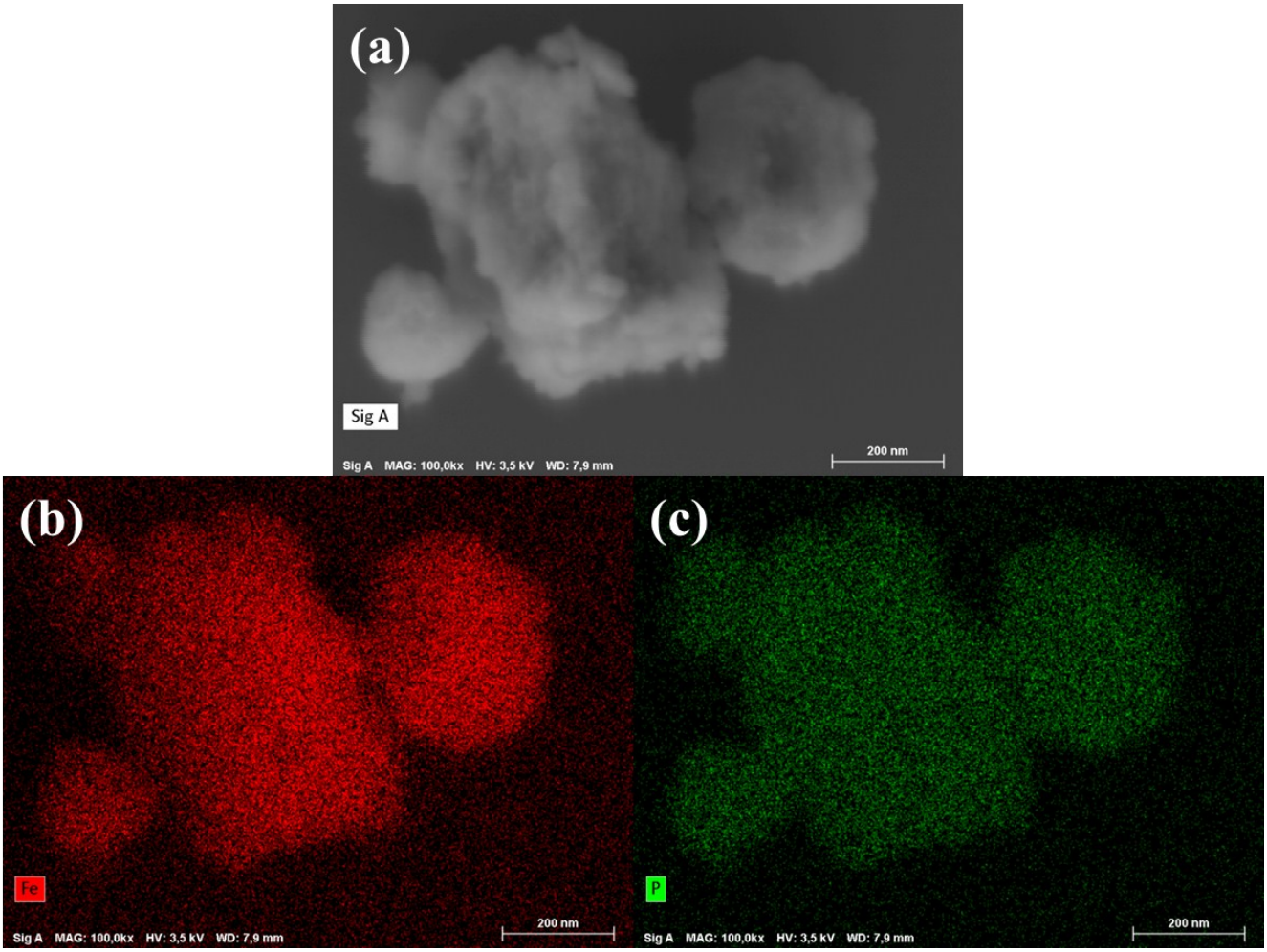

Figure S21. (a) SEM image of as-synthesized FeP. The EDX mapping carried out on (a) displayed the homogenous distribution of iron (b) and phosphorous (c) in the structure (scale bar 200 nm).

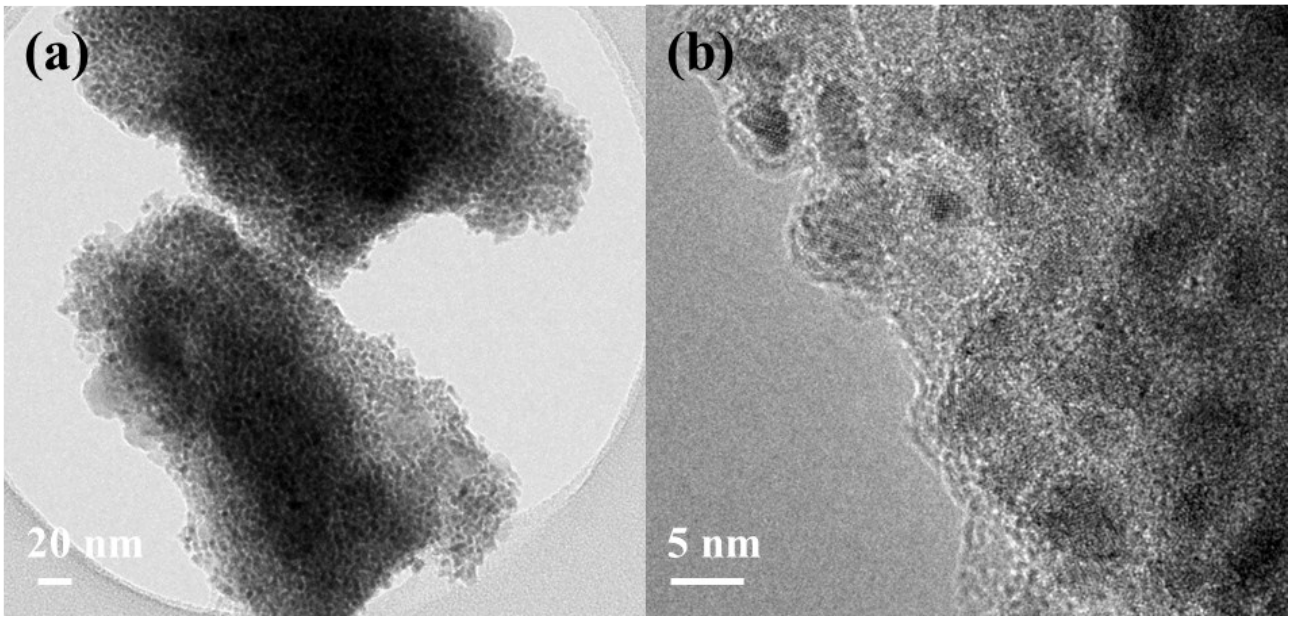

Figure S22. (a) TEM and (c) High resolution (HR) TEM image of and FeP nanoparticles. The as-synthesized nanoparticles were in the range of 2-5 nm as revealed by HR TEM (see also Figure 3 in the main text)

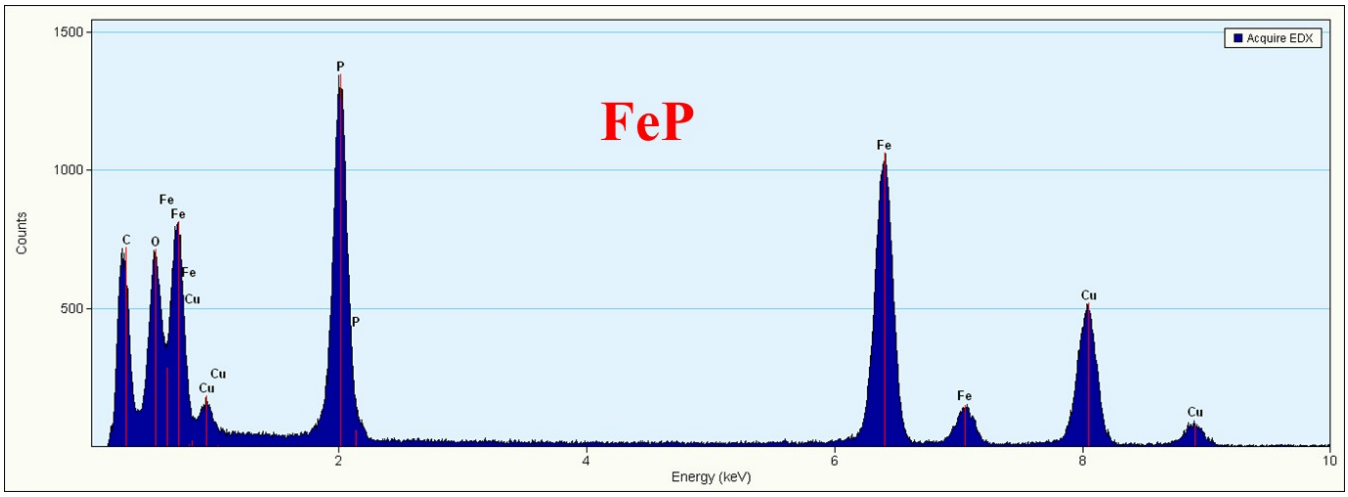

Figure S23. The presence of iron and phosphorous in FeP was also determined by the EDX analysis (see Table S11). The appearance of peaks for copper is due to the TEM grid (carbon film on 300 mesh Cu-grid).

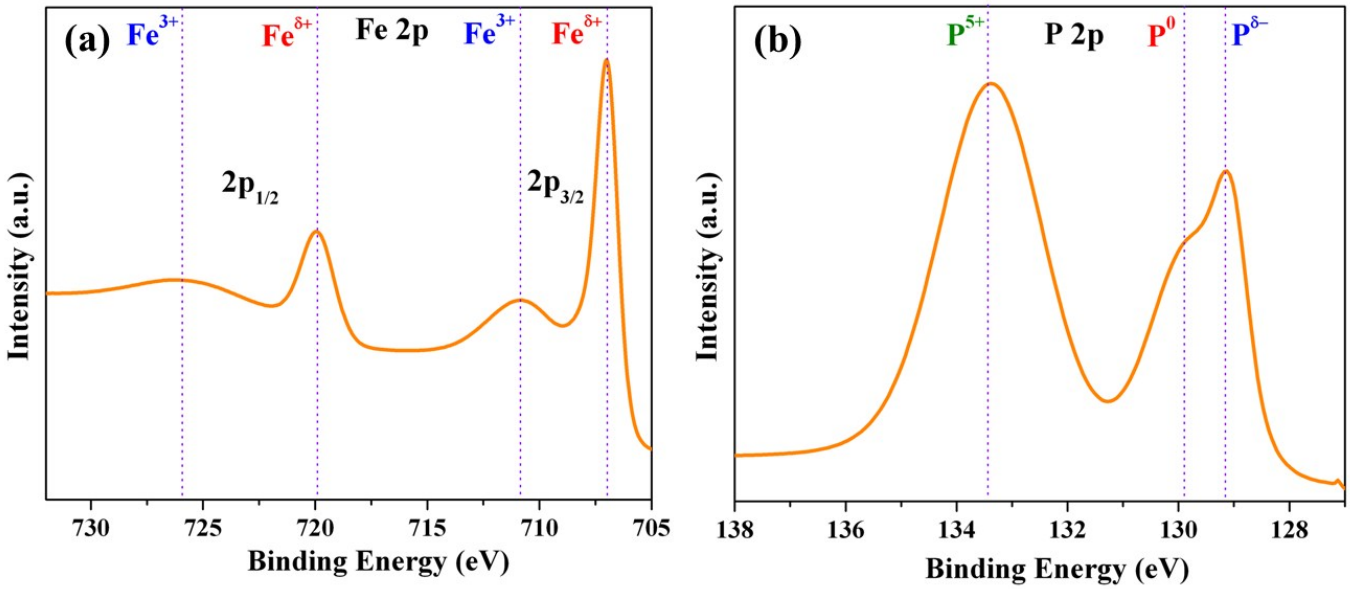

Figure S24. The surface chemical states of FeP were analyzed by XPS spectroscopy. (a) and (b) shows the high-resolution XPS spectra of Fe 2p and P 2p. In the Fe $2p_{3/2}$ and $2p_{1/2}$ exhibited two major and two minor peaks. The peaks at the binding energy of 707 and 719.9 eV could be assigned to $Fe^{\delta+}$ which is slightly more positive than Fe^0 ($2p_{3/2}$:706.6 eV) and originated from the Fe–P bonding structures from iron phosphide, in good agreement with previous reports.[29–31] The other two peaks at 710.9 and 725.4 eV can be ascribed to the oxidized state of Fe (Fe^{3+}) due to the surface passivation and is a common phenomenon in metal phosphides. The P 2p XPS spectrum exhibited three peaks. The broad peak at 129 eV is assigned to the $P^{\delta-}$ while the peak at ~130 corresponds to the P^0. This shows that P in FeP has a slightly -ve charge.[29–31] It has been observed that in hydrogenase and its analogues the hydride acceptor has a small +ve charge whereas the proton acceptor has small -ve charge, and they act as the vital active sites to catalyze HER.[32] This was already an indication that weakly charged Fe and P in FeP could be an apt material for OER and HER, and for overall water splitting.[33] The third peak at 133.4 could be ascribed to the oxidized P species upon the exposure to air, as also observed for other iron phosphide catalysts reported previously.[34]

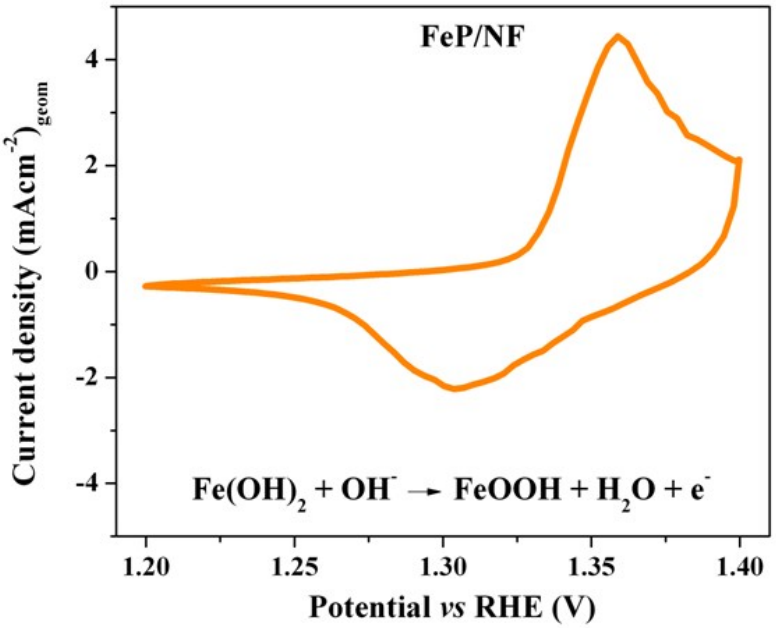

Figure. S25. CV (sweep rate 1 mV/s) of FeP/NF measured between 1.2 to 1.4 V (vs RHE) in 1 M KOH featuring a small pair of anodic and cathodic peaks corresponding to the reaction $Fe(OH)_2 + OH^- \rightarrow FeOOH + H_2O + e^-$.[35] The voltammogram suggests that the surface of FeP is oxidized to higher valance state of Fe, which indeed serves as catalytically active site for the OER.

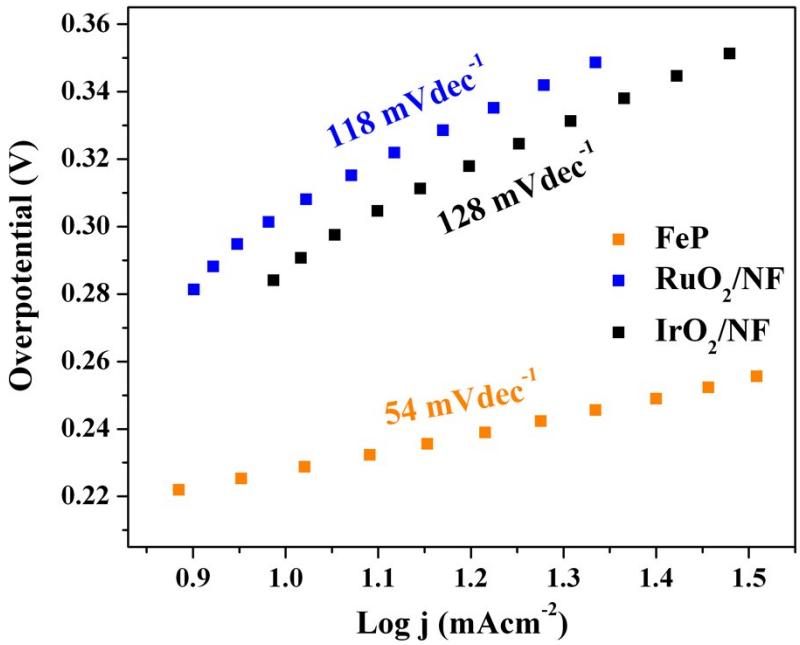

Figure. S26. Comparison of the Tafel plot of FeP/NF and noble-metal based catalysts measured with a scan rate of 1 mVs^{-1} in aqueous 1 M KOH solution. A small Tafel slope of 54 $mVdec^{-1}$ was attained for FeP/NF showing favourable reaction kinetics of OER.

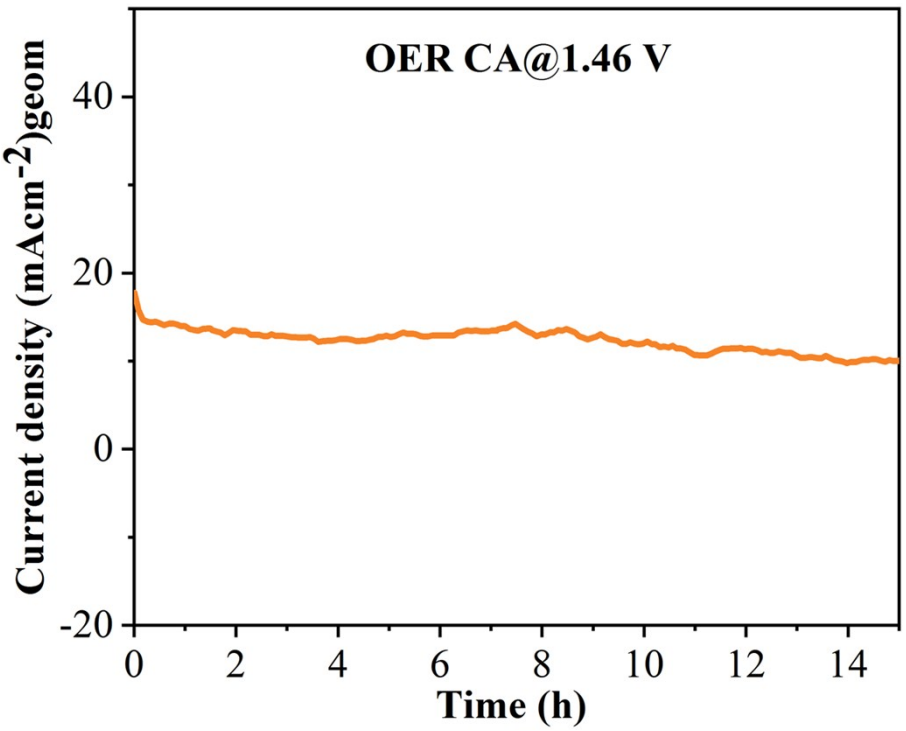

Figure S27. The CA responses of amorphous FeP on NF measured in OER conditions at a potential of 1.46 V (vs RHE) in aqueous 1 M KOH solution. The catalyst was strikingly stable for more than 15 h.

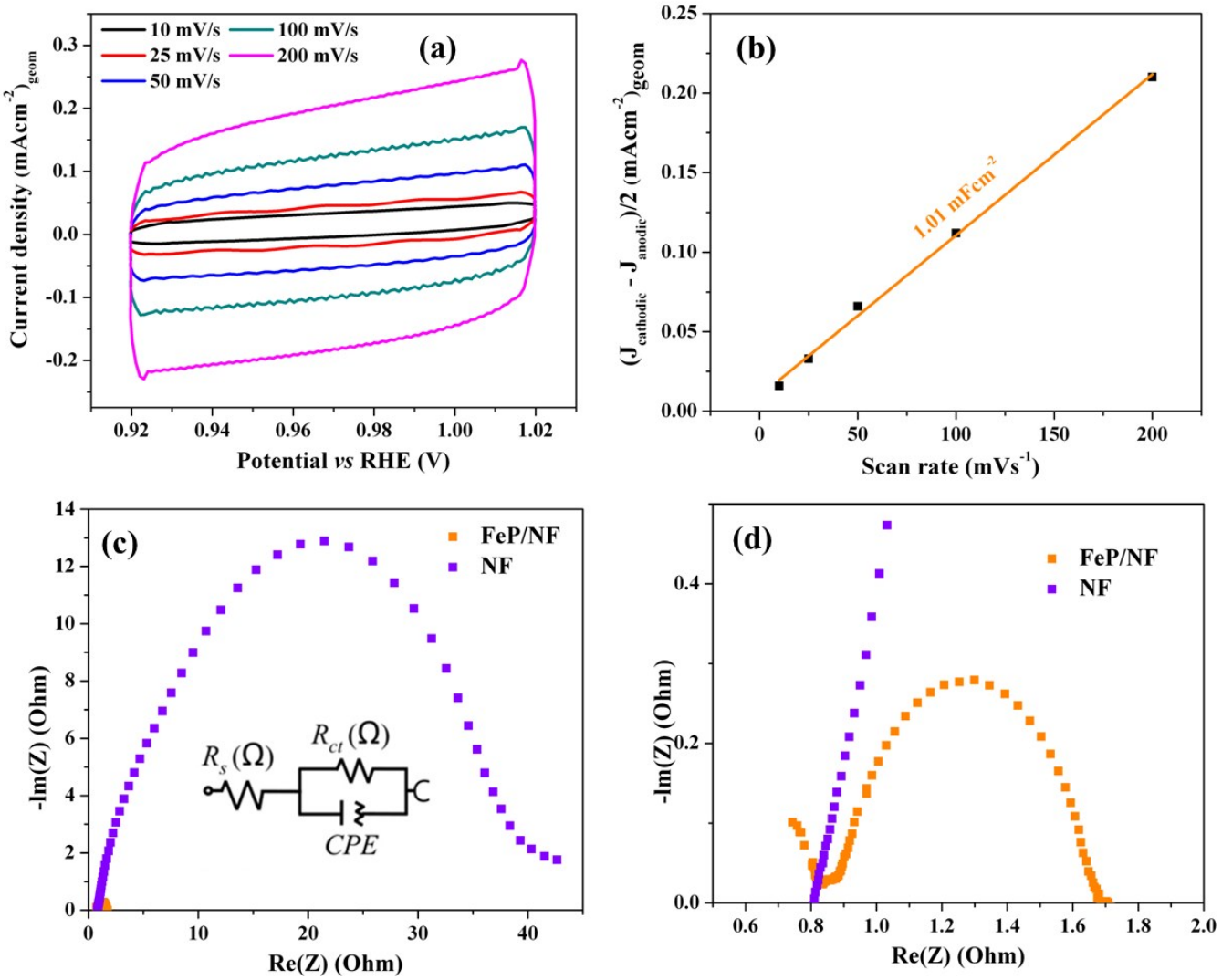

Figure S28. ECSA analysis by the CV scans in a non-Faradaic potential range of as-prepared FeP/NF electrodes in 1 M KOH at scan rate of 10 mV/s, 25 mV/s, 50 mV/s, 100 mV/s and 200 mV/s (a). Half of the differences in current density variation ($\Delta J = (J_{cathodic}-J_{anodic})/2$) at a potential of 0.05 V vs RHE plotted against scan rate fitted to a linear regression that allows the determination of double layer capacitance (C_{dl}). The C_{dl} value attained for FeP/NF was 1.01 $mFcm^{-2}$ (b). The ECSA was then calculated by using the C_{dl} and the specific capacitance of the material (C_s) per unit area, and a value of 0.6 cm^2 was estimated providing the information on the catalytic active sites favoring the efficient adsorption and transfer of reactants to enhance the electrochemical reaction. The Nyquist plots obtained from EIS are presented in (c) and the respective Randles equivalent circuit model is shown in the inset where R_s is the equivalent series resistance, CPE is the constant phase element of the double-layer capacitance and R_{ct} is the charge transfer resistance, respectively. The zoomed plot (d) showed significantly reduced charge transfer resistance (R_{ct}) for FeP/NF compared to bare NF, indicating the rapid charge transfer process.

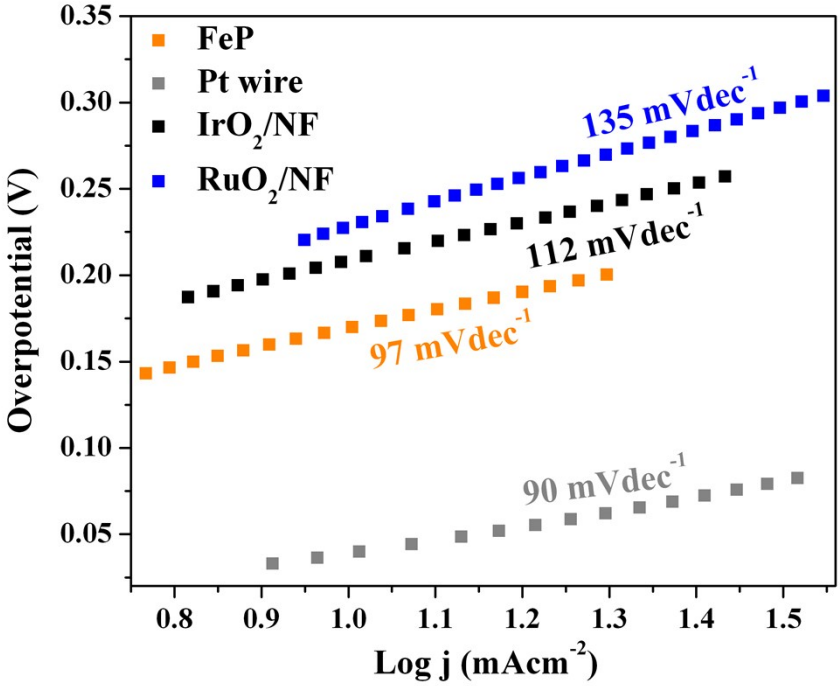

Figure. S29. Comparison of the Tafel plot of FeP/NF and noble-metal based catalysts measured with a scan rate of 1 mVs^{-1} in aqueous 1 M KOH solution for HER. The obtained Tafel slope of 97 $mVdec^{-1}$ for HER suggests that the reaction takes place on FeP surface via a Volmer-Heyrovsky mechanism.[36]

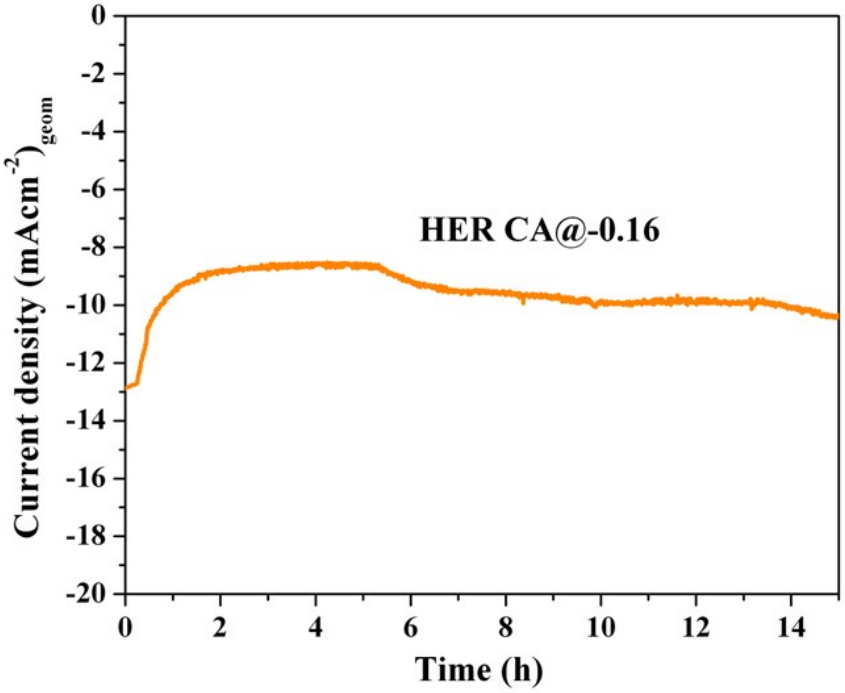

Figure S30. The CA responses of amorphous FeP on NF measured in HER conditions at a potential of -0.16 V (vs RHE) in aqueous 1 M KOH solution. The catalyst was highly stable for more than 15 h.

Table S12. The comparison of OER overpotentials of FeP with other superior selected non-noble catalysts 1 M KOH (pH 14).

Catalyst	Current density ($mAcm^{-2}$)	Overpotential (mV)	Reference
FeP /NF	**10**	**227**	**This work**
	100	**292**	**This work**
FeP/Au	10	290	[37]
FeP RGO/Au	10	260	[37]
FeMnP	10	250	[38]
FeP	10	288	[39]
Ni_2P/NF	10	240	[40]
$Ni_{12}P_5$/NF	10	260	[40]
MoO_2/NF	10	250	[41]
MoO_2/NF compact	10	500	[41]
$Ni(OH)_2$/NF	10	330	[42]
Ni-P	10	300	[43]
NiCo-MOF	10	250	[44]
NiFe-MOF	10	240	[45]
Ni_2P/FTO	10	400	[46]
Ni_2P/FTO	10	500	[46]
Ni_2P/Ni/NF	10	200	[47]
Ni_xP_y-325	10	320	[48]
Ni_2P/GC	10	290	[49]
Ni_5P_4 films	10	290	[50]
Ni-P film	10	344	[51]
Co-P/Cu	10	345	[52]
Ni_3S_2/NF	10	250	[53]
NiSe/NF	10	215	[54]
$Ni_{1-x}Fe_x$ NC/GC	10	330	[55]
Co_3O_4/ $NiCo_2O_4$ DSNCs	10	340	[56]
CoP/Cu	10	345	[51]
CoCo LDH	10	393	[57]
CoO_x/CN	10	260	[58]
FeOOH/CeO_2/NF	10	250	[59]
$NiFeO_x$	10	350	[60]
Co_3O_4@CoP	10	238	[61]
CoP/NCNHP	10	310	[62]
Ni_2P/Ni_3S_2	10	210	[63]
FeCH@GDY/NF	10	268	[64]
$Fe_{17.5\%}$-Ni_3S_2/NF	10	214	[65]

Table S13. The comparison of HER overpotentials of FeP with other highly active selected non-noble catalysts in 1 M KOH (pH 14).

Catalyst	Current density ($mAcm^{-2}$)	Overpotential (mV)	Reference
FeP /NF	**-10**	**165**	**This work**
	-100	**286**	**This work**
CoS_2	-10	175	[66]
FeP	-10	144	[39]
FeP	-10	194	[29]
FeP_2	-10	189	[29]
CoMo	-10	170	[67]
CoS_2	-10	145	[68]
CoN_x	-10	140	[69]
Mo_2C	-10	130	[70]
Ni-NS	-10	80	[71]
$Ni(OH)_2$/NF	-10	172	[42]
Ni/Mo_2C-PC	-10	179	[72]
$Co(S_xSe_{1-x})_2$	-10	130	[73]
Ni_2P	-10	87	[74]
Ni_2P/NF	-10	85	[40]
$Ni_{12}P_5$/NF	-10	170	[40]
Ni-P electrodeposited	-10	93	[51]
Ni_2P/GC	-10	220	[49]
Ni_xP_y-325	-20	160	[48]
Ni_2P/GEC	-20	205	[74]
NiFe LDH/NF	-10	200	[75]
Ni-NiO	-10	250	[76]
Ni_2P/GC	-20	250	[77]
Ni_5P_4 film	-10	180	[50]
$NiCo_2S_4$	-20	194	[78]
Ni_3S_2/NF	-10	220	[53]
Ni NC/GC	-10	219	[55]
CoO_x/CN	-10	232	[58]
CoO_x/CN	-20	352	[58]
CoNR CNT	-10	370	[79]
CoMn-S@NiO/CC	-100	232	[48]
CoP nanowire	-20	335	[80]
CoNiP/NF	-10	155	[46]
CoP/CC	-10	209	[80]
MoC_x/C	-20	189	[81]
CoP/NCNHP	-10	115	[62]
Ni_2P/Ni_3S_2	-10	80	[63]
FeCH@GDY/NF	-10	148	[64]
$Fe_{17.5\%}$-Ni_3S_2/NF	-10	47	[65]

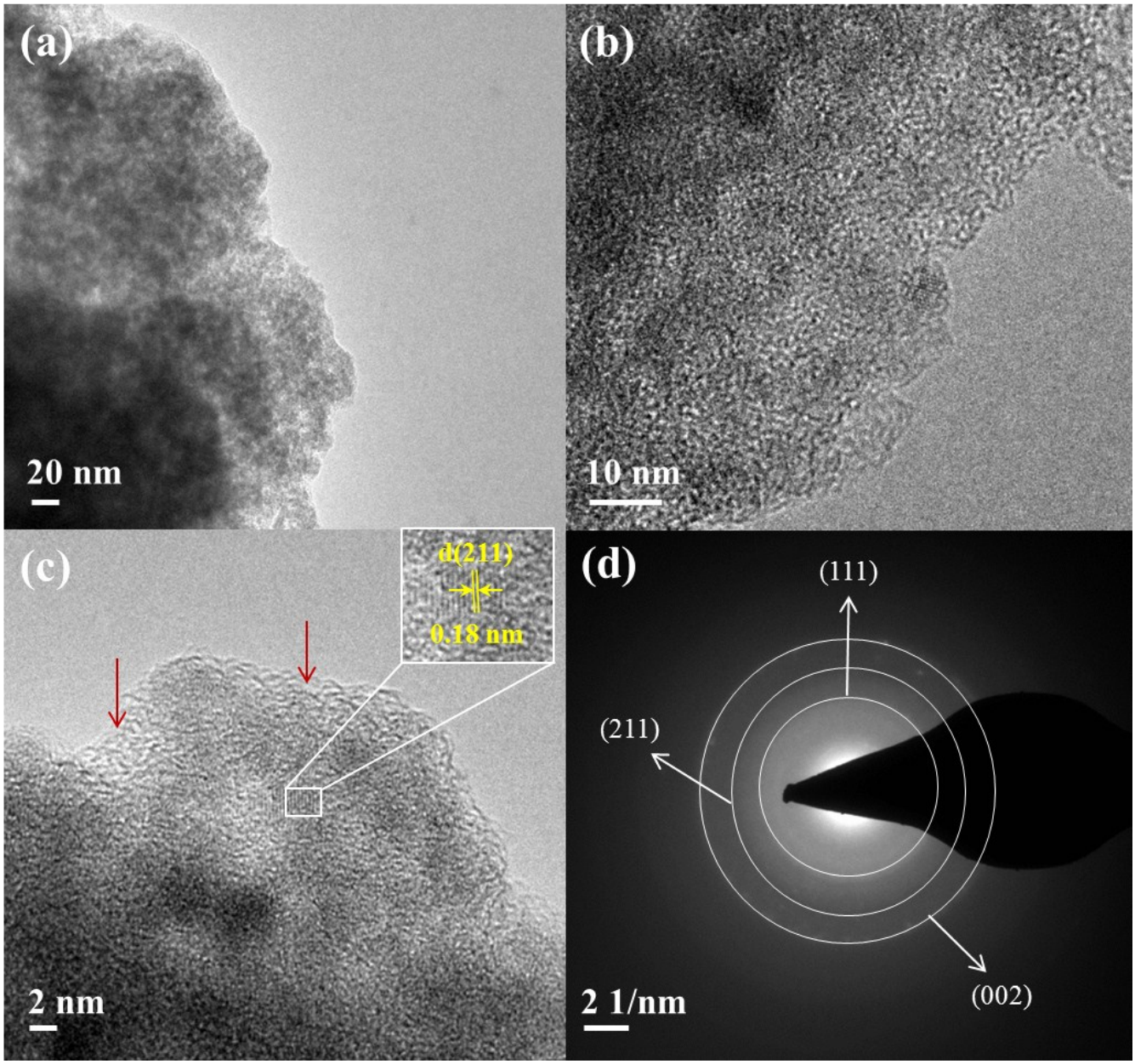

Figure S31. (a, b) TEM (c) HR-TEM and (d) selected area electron diffraction (SAED) images of the thin films of FeP after the oxygen evolution (OER CA) measurements in aqueous 1 M KOH solution for 15 h. The HR-TEM image showed the destruction of the surface with amorphous nature of the particles (red arrows) under electrochemical and strongly alkaline conditions which could be attributed to the loss of a large amount of phosphorus (as detected from ICP-AES and EDX analysis) from surface forming $Fe(OH)_2$/FeOOH phase with defects and disorders. This phenomenon has been well documented in the literature for the first-row transition metal-based materials investigated for OER catalysis. The core of the particle was still crystalline and showed lattice spacing of 0.18 nm corresponding to the (211) plane of FeP (see (c) inset). The SAED (d) patterns revealed rings with a lattice spacing of 0.24 nm, 0.18 nm and 0.15 nm corresponding to (111), (211) and (002) planes, respectively.[28]

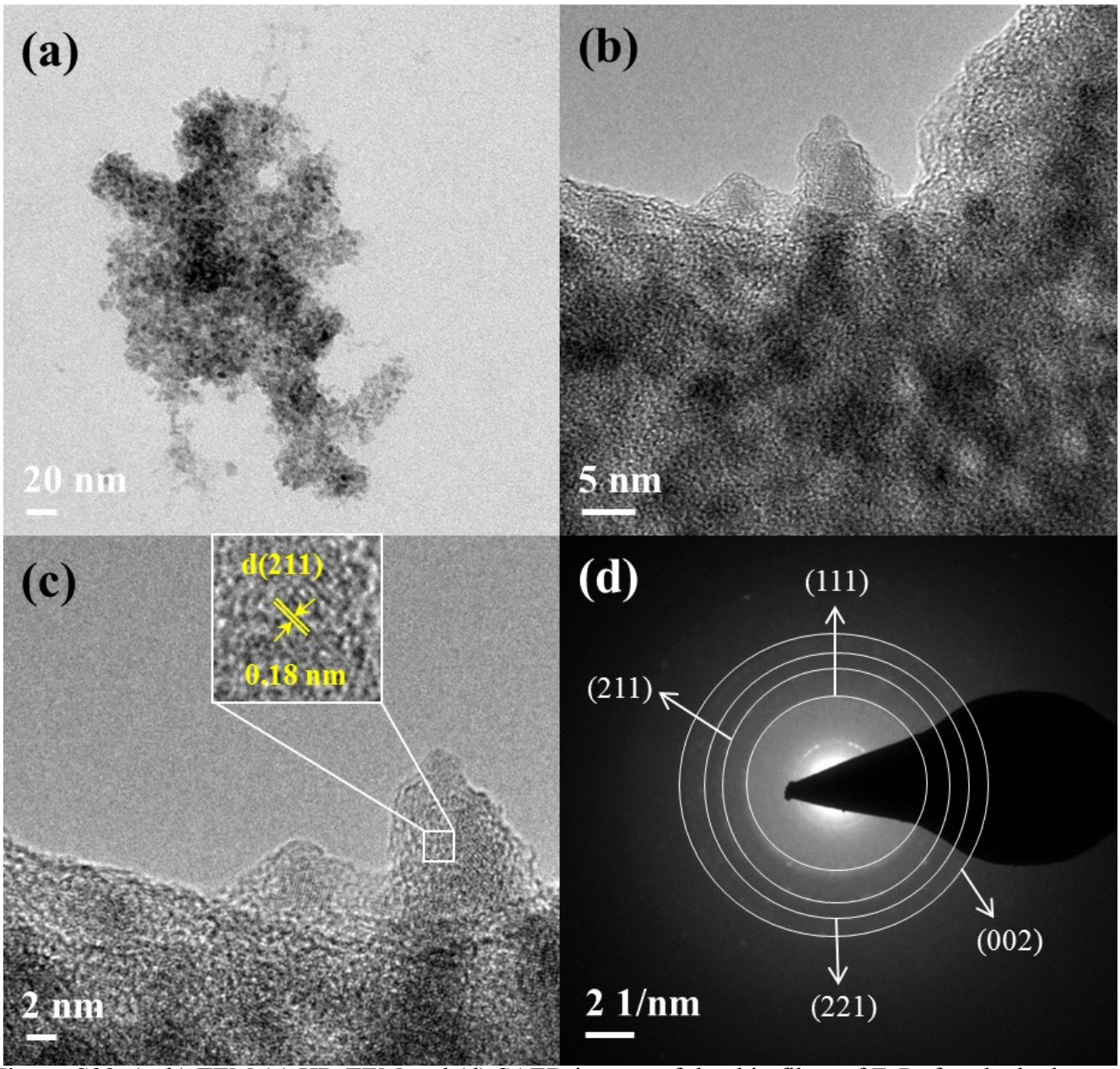

Figure S32. (a, b) TEM (c) HR-TEM and (d) SAED images of the thin films of FeP after the hydrogen evolution (HER CA) measurements in aqueous 1 M KOH solution for 15 h. From the HR-TEM, it was found that the FeP was well crystalline and a clear lattice spacing of 0.18 nm (Figure (c) inset) corresponding to (211) plane of FeP were observed. Slight amount of loss of phosphorus was also apparent from ICP-AES, EDX and XPS analysis which is unavoidable due to the strongly alkaline conditions and has been previously reported numerous phosphide-based materials. The SAED (c) patterns revealed rings with a lattice spacing of 0.24 nm, 0.18 nm, 0.16 nm, and 0.15 nm corresponding to (111), (211), (221), and (002) planes, respectively.[28]

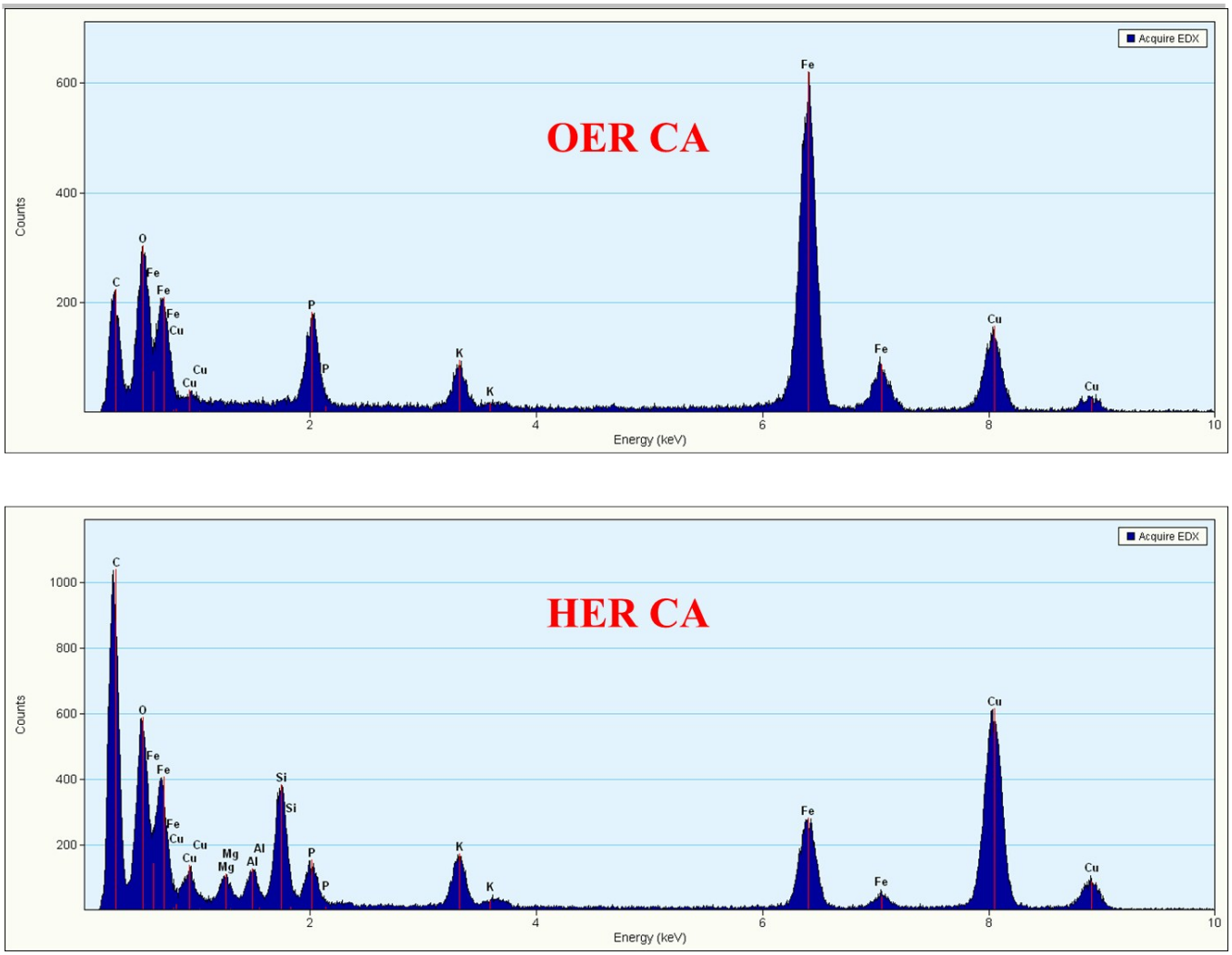

Figure S33. The presence of iron and phosphorous in FeP after OER CA and HER CA was also determined by the EDX analysis (see Table S11). The appearance of peaks for Cu is due to the TEM grid (carbon film on 300 mesh Cu-grid) and the Si and Mg are due to the FTO substrate. The source of potassium in the spectra is from the electrolyte.

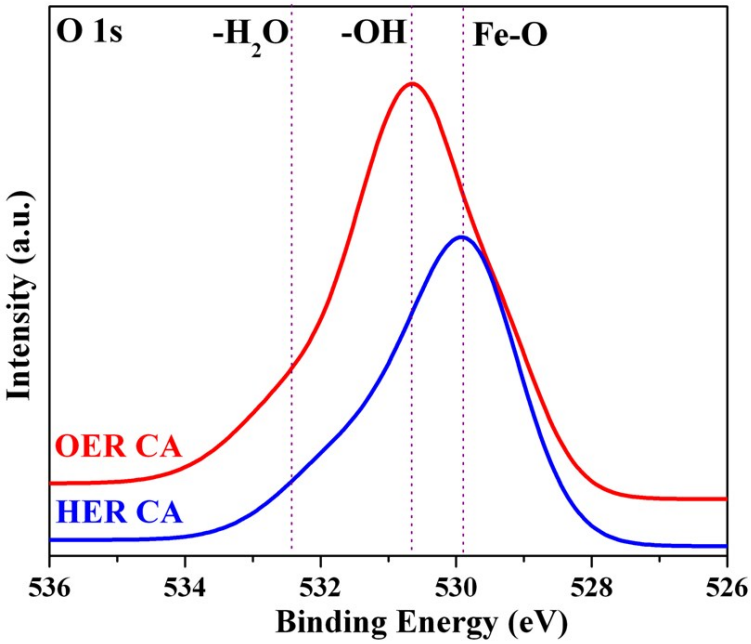

Figure S34. The O1s XPS spectra of FeP after OER CA (red) and HER CA (blue). The O1s spectra in OER CA showed a broad peak 530.8 eV could be assigned to oxygen in –OH groups, indicating the surface of the material is hydroxylated due to the consequence of either surface hydroxides or substitution of oxygen atoms at the surface by hydroxyl groups whereas the broader shoulder at around 532.4 eV can be ascribed to adsorbed water. The O1s spectra of HER CA displayed a peak at 529. 9 eV which could be ascribed to the metal–oxygen bonds of iron oxide.[82,83] In addition to this, the broad peak also appeared corresponding to the formation of the surface hydroxyl group. The presented binding energies can be well matched with similar literature reported examples based on iron.[40,84,85]

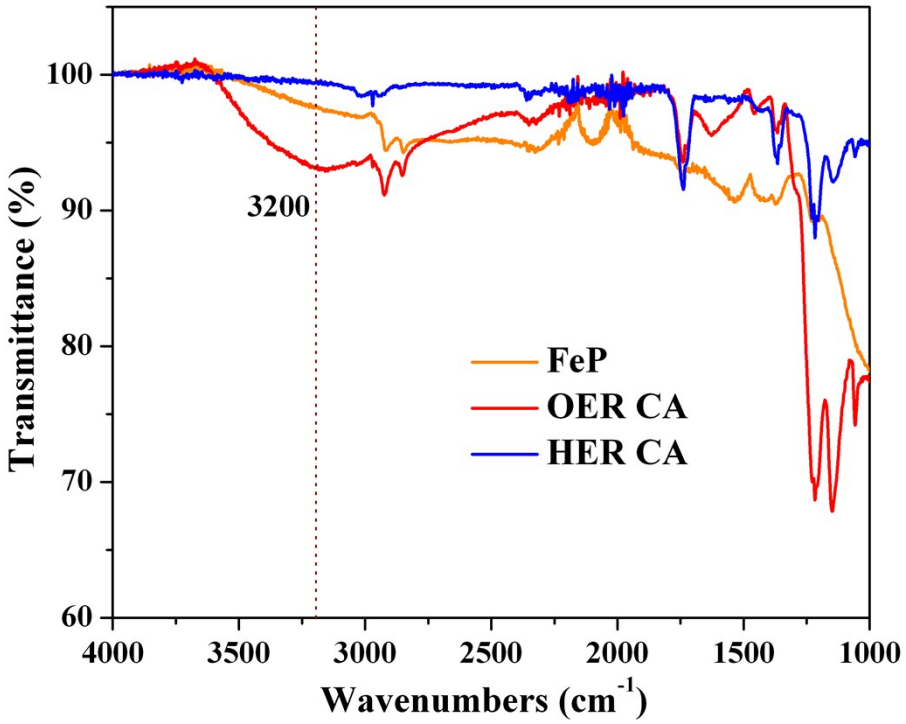

Figure S35. FT-IR transmission spectrum of as-prepared FeP, FeP after OER CA and HER CA. The OER CA sample showed a broad band at ~ 3200 that could be assigned to H stretching. This indicates that FeP was largely hydroxylated after OER CA.

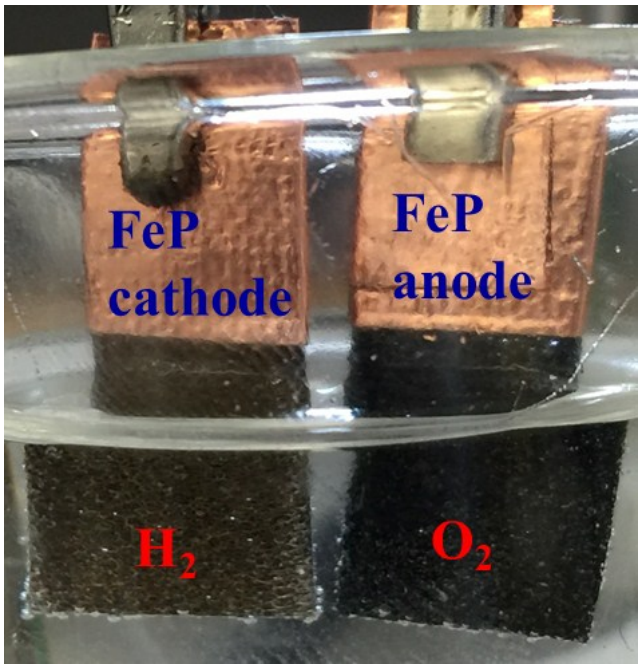

Figure S36. Overall water-splitting with FeP‖FeP on NF in 1 M KOH solution. Vigorous bubble formation was observed during the experiment.

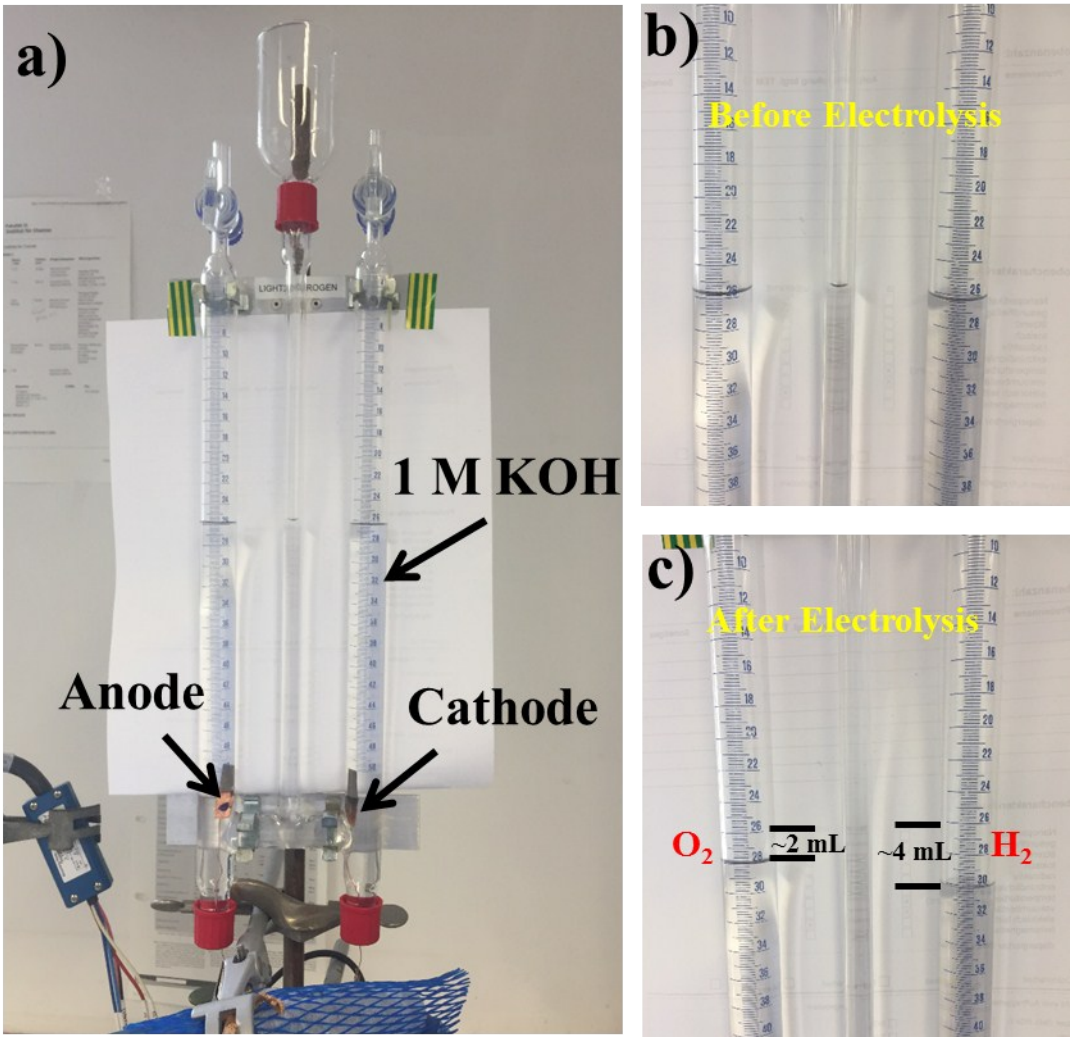

Figure S37. a) An inverted two-electrode FeP‖FeP electrolyzer was used at a constant current density of 10 $mAcm^{-2}$ in 1 M KOH to allow the collection of H_2 and O_2 separately at atmospheric pressure. b) The initial level of the electrolyte was noted and then the valves were closed. During electrolysis, as a result of evolution and collection of H_2 and O_2 at the upper part of the cell, the level of electrolyte goes down and the change in volume over time was noted. c)The ratio of volumes of H_2 and O_2 remained almost 2:1 over one hour of electrolysis.

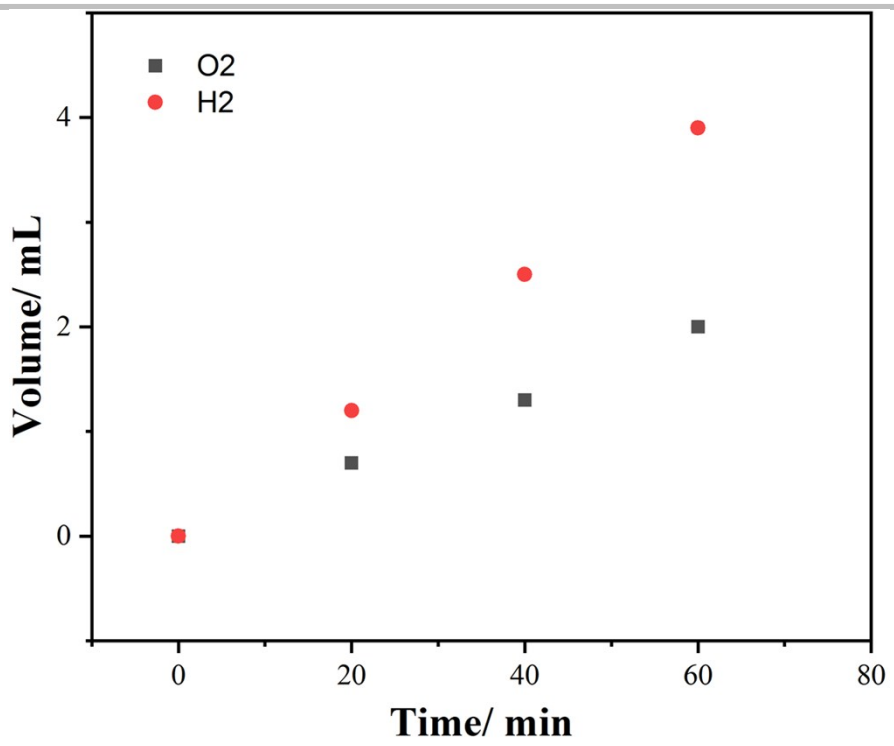

Figure S38. The plot of volume change as result of H_2 and O_2 evolution in the experiments of Figure S37 with respect to time. The ratios of H_2 and O_2 were obtained from the modified two electrodes of FeP‖FeP on NF as both cathode and anode in 1 M KOH solution at a current of 10 $mAcm^{-2}$ for 1 h. The attained ratios directly confirmed the evolution of gases as well as the amount of H_2 was approximately twice larger than the O_2 demonstrating the efficient selectivity and reactivity of the catalysts.

Calculation of Faradaic efficiency

The Faradaic efficiency (FE) of FeP in 1M KOH towards oxygen and hydrogen evolution reaction was measured in a two-electrode configuration where nickel foam loaded with FeP were used as both cathode and anode in a closed electrochemical cell. The electrolyte and cell were first degassed with Argon for 30 min under stirring. Afterwards, constant current density of 10 $mAcm^{-2}$ was applied for a certain period of time. At the end of electrolysis, the gaseous samples were drawn from the head space by a gas tight syringe and analyzed by a GC calibrated for H_2, and O_2. Each injection was repeated at least three times and the average value is presented.

The Faradaic efficiency (FE) is calculated based on:

$$FE(H_2,\%) = \frac{V_{H_2} \times 2 \times F}{V_m \times j \times t} \times 100\%$$

$$FE(O_2,\%) = \frac{V_{O_2} \times 4 \times F}{V_m \times j \times t} \times 100\%$$

V_{H2}, V_{O2} is the evolved volume of hydrogen and oxygen, F is the Faraday constant (96485.33289 C/mol), V_m is the molar volume of the gas, j is the current density (10 $mAcm^{-2}$) and t is the time period of electrolysis.

Table S14: Calculation of Faradaic efficiency

	***j* /mAcm^{-2}**	***t*/ sec**	***V_{H2}*/ mL**	***V_{O2}*/ mL**	***V_{H2}*:*V_{O2}***	***FE (H_2,%)***	***FE (O_2,%)***
FeP	10	360	0.41	0.20	2.05:1	99	96

E. References

1 S. Yao, T. Szilvási, N. Lindenmaier, Y. Xiong, S. Inoue, M. Adelhardt, J. Sutter, K. Meyer and M. Driess, *Chem. Commun.*, 2015, **51**, 6153–6156.

2 D. F. Evans, *J. Chem. Soc.*, 1959, 2003–2005.

3 T. Ayers, R. Turk, C. Lane, J. Goins, D. Jameson and S. J. Slattery, *Inorganica Chim. Acta*, 2004, **357**, 202–206.

4 G. M. Sheldrick, *SHELX-97 Program for Crystal Structure Determination*, Universität Göttingen, Germany, 1997.

5 F. De Proft, C. Van Alsenoy, A. Peeters, W. Langenaeker and P. Geerlings, *J. Comput. Chem.*, 2002, **23**, 1198–1209.

6 N. Schuth, S. Mebs, D. Huwald, P. Wrzolek, M. Schwalbe, A. Hemschemeier, N. Schuth, S. Mebs, D. Huwald, P. Wrzolek, M. Schwalbe and A. Hemschemeier, *Proc. Natl. Acad. Sci.*, 2017, **114**, 8556–8561.

7 A. Petuker, S. Mebs, N. Schuth, P. Gerschel, M. L. Reback, B. Mallick, M. van Gastel, M. Haumann and U.-P. Apfel, *Dalt. Trans.*, 2017, **46**, 907–917.

8 S. Yao, F. Meier, N. Lindenmaier, R. Rudolph, B. Blom, M. Adelhardt, J. Sutter, S. Mebs, M. Haumann, K. Meyer, M. Kaupp and M. Driess, *Angew. Chemie - Int. Ed.*, 2015, **54**, 12506–12510.

9 J. J. Rehr, J. J. Kas, F. D. Vila, M. P. Prange and K. Jorissen, *Phys. Chem. Chem. Phys.*, 2010, **12**, 5503–5513.

10 J. Tao, J. P. Perdew, V. N. Staroverov and G. E. Scuseria, *Phys. Rev. Lett.*, 2003, **91**, 146401–146404.

11 A. Schäfer, C. Huber, R. Ahlrichs, A. Schafer, C. Huber and R. Ahlrichs, *J. Chem. Phys.*, 1994, **100**, 5829–5835.

12 M. J. Frisch, G. W. Trucks, H. B. Schlegel, G. E. Scuseria, M. A. Robb, J. R. Cheeseman, G. Scalmani, V. Barone, B. Mennucci, G. A. Petersson, H. Nakatsuji, M. Caricato, X. Li, H. P. Hratchian, A. F. Izmaylov, J. Bloino, G. Zheng, J. L. Sonnenberg, M. Had, J. Cioslowski and D. J. Fox, 2009.

13 F. B. Biegler-Konig, J. Schonbohm and D. Bayles, *J. Comput. Chem.*, 2001, **22**, 545–559.

14 E. R. Johnson, S. Keinan, P. Mori Sánchez, J. Contreras García, A. J. Cohen and W. Yang, *J. Am. Chem. Soc.*, 2010, **132**, 6498–6506.

15 F. Neese, *WIREs Comput Mol Sci*, 2012, **2**, 73–78.

16 I. Mayer, *Chem.Phys.Lett.*, 1983, **97**, 270–274.

17 F. Neese, *J. Phys. Chem. Solids*, 2004, **65**, 781–785.

18 C. B. Hübschle and P. Luger, *J. Appl. Crystallogr.*, 2006, **39**, 901–904.

19 J. Yu, Y. Zhong, X. Wu, J. Sunarso, M. Ni, W. Zhou and Z. Shao, *Adv. Sci.*, 2018, 1800514.

20 Q. Kang, L. Vernisse, R. C. Remsing, A. C. Thenuwara, S. L. Shumlas, I. G. McKendry, M. L. Klein, E. Borguet, M. J. Zdilla and D. R. Strongin, *J. Am. Chem. Soc.*, 2017, **139**, 1863–1870.

21 Y. Liu, G. Yu, G. D. Li, Y. Sun, T. Asefa, W. Chen and X. Zou, *Angew. Chemie - Int. Ed.*, 2015, **54**, 10752–10757.

22 X. Lu, W.-L. Yim, B. H. R. Suryanto and C. Zhao, *J. Am. Chem. Soc.*, 2015, **137**, 2901–2907.

23 H. Liang, A. N. Gandi, D. H. Anjum, X. Wang, U. Schwingenschlögl and H. N. Alshareef, *Nano Lett.*, 2016, **16**, 7718–7725.

24 J. M. Smith, A. R. Sadique, T. R. Cundari, K. R. Rodgers, G. Lukat-Rodgers, R. J. Lachicotte, C. J. Flaschenriem, J. Vela and P. L. Holland, *J. Am. Chem. Soc.*, 2006, **128**, 756–769.

25 R. S. Mulliken, *J. Chem. Phys.*, 1955, **23**, 1833–1840.

26 R. W. F. Bader, *Atoms in Molecules: A Quantum Theory*, Cambridge University Press: Oxford, U.K., 1991.

27 J. Contreras-García, E. R. Johnson, S. Keinan, R. Chaudret, J. P. Piquemal, D. N. Beratan and W. Yang, *J. Chem. Theory Comput.*, 2011, **7**, 625–632.

28 K. Selte and A. Kjekshus, *Acta Chem. Scand.*, 1972, 26, 1276–1277.

29 C. Y. Son, I. H. Kwak, Y. R. Lim and J. Park, *Chem. Commun.*, 2016, **52**, 2819–2822.
30 D. Xiong, X. Wang, W. Li and L. Liu, *Chem. Commun.*, 2016, **52**, 8711–8714.
31 C. Lv, Z. Chen, Z. Chen, B. Zhang, Y. Qin, Z. Huang and C. Zhang, *J. Mater. Chem. A*, 2015, **3**, 17669–17675.
32 P. Liu and J. A. Rodriguez, *J. Am. Chem. Soc.*, 2005, **127**, 14871–14878.
33 J. F. Callejas, J. M. McEnaney, C. G. Read, J. C. Crompton, A. J. Biacchi, E. J. Popczun, T. R. Gordon, N. S. Lewis and R. E. Schaak, *ACS Nano*, 2014, **8**, 11101–11107.
34 L. Jin, H. Xia, Z. Huang, C. Lv, J. Wang, M. G. Humphrey and C. Zhang, *J. Mater. Chem. A*, 2016, **4**, 10925–10932.
35 C. Panda, P. W. Menezes, C. Walter, S. Yao, M. E. Miehlich, V. Gutkin, K. Meyer and M. Driess, *Angew. Chemie - Int. Ed.*, 2017, **56**, 10506–10510.
36 H. Li, P. Wen, Q. Li, C. Dun, J. Xing, C. Lu, S. Adhikari, L. Jiang, D. L. Carroll and S. M. Geyer, *Adv. Energy Mater.*, 2017, **7**, 1700513.
37 J. Masud, S. Umapathi, N. Ashokaan and M. Nath, *J. Mater. Chem. A*, 2016, **4**, 9750–9754.
38 D. Li, H. Baydoun, B. Kulikowski and S. L. Brock, *Chem. Mater.*, 2017, **29**, 3048–3054.
39 Y. Yan, B. Y. Xia, X. Ge, Z. Liu, A. Fisher and X. Wang, *Chem. - A Eur. J.*, 2015, **21**, 18062–18067.
40 P. W. Menezes, A. Indra, C. Das, C. Walter, C. Göbel, V. Gutkin, D. Schmeißer and M. Driess, *ACS Catal.*, 2017, **7**, 103–109.
41 Y. Jin, H. Wang, J. Li, X. Yue, Y. Han, P. K. Shen and Y. Cui, *Adv. Mater.*, 2016, **28**, 3785–3790.
42 Y. Rao, Y. Wang, H. Ning, P. Li and M. Wu, *ACS Appl. Mater. Interfaces*, 2016, **8**, 33601–33607.
43 X.-Y. Yu, Y. Feng, B. Guan, X. W. (David) Lou and U. Paik, *Energy Environ. Sci.*, 2016, **9**, 1246–1250.
44 S. Zhao, Y. Wang, J. Dong, C.-T. He, H. Yin, P. An, K. Zhao, X. Zhang, C. Gao, L. Zhang, J. Lv, J. Wang, J. Zhang, A. M. Khattak, N. A. Khan, Z. Wei, J. Zhang, S. Liu, H. Zhao and Z. Tang, *Nat. Energy*, 2016, **1**, 16184.
45 J. Duan, S. Chen and C. Zhao, *Nat. Commun.*, 2017, **8**, 15341.
46 A. Han, H. Chen, Z. Sun, J. Xu and P. Du, *Chem. Commun.*, 2015, **51**, 11626–11629.
47 B. You, N. Jiang, M. Sheng, M. W. Bhushan and Y. Sun, *ACS Catal.*, 2016, **6**, 714–721.
48 Q. Li, Z. Xing, D. Wang, X. Sun and X. Yang, *ACS Catal.*, 2016, **6**, 2797–2801.
49 L.-A. Stern, L. Feng, F. Song and X. Hu, *Energy Environ. Sci.*, 2015, **8**, 2347–2351.
50 M. Ledendecker, S. Krickcalderõn, C. Papp, H. P. Steinrück, M. Antonietti and M. Shalom, *Angew. Chemie - Int. Ed.*, 2015, **54**, 12361–12365.
51 N. Jiang, B. You, M. Sheng and Y. Sun, *ChemCatChem*, 2016, **8**, 106–112.
52 N. Jiang, B. You, M. Sheng and Y. Sun, *Angew. Chemie - Int. Ed.*, 2015, **54**, 6251–6254.
53 L. L. Feng, G. Yu, Y. Wu, G. D. Li, H. Li, Y. Sun, T. Asefa, W. Chen and X. Zou, *J. Am. Chem. Soc.*, 2015, **137**, 14023–14026.
54 X. Lu and C. Zhao, *Nat. Commun.*, 2015, **6**, 6616.
55 X. Zhang, H. Xu, X. Li, Y. Li, T. Yang and Y. Liang, *ACS Catal.*, 2016, **6**, 580–588.
56 H. Hu, B. Guan, B. Xia and X. W. Lou, *J. Am. Chem. Soc.*, 2015, **137**, 5590–5595.
57 F. Song and X. Hu, *Nat. Commun.*, 2014, **5**, 4477.
58 H. Jin, J. Wang, D. Su, Z. Wei, Z. Pang and Y. Wang, *J. Am. Chem. Soc.*, 2015, **137**, 2688–2694.
59 J.-X. Feng, S.-H. Ye, H. Xu, Y.-X. Tong and G.-R. Li, *Adv. Mater.*, 2016, **28**, 4698–4703.
60 C. C. L. McCrory, S. Jung, J. C. Peters and T. F. Jaramillo, *J. Am. Chem. Soc.*, 2013, **135**, 16977–16987.
61 J. Zhou, Y. Dou, A. Zhou, R. M. Guo, M. J. Zhao and J. R. Li, *Adv. Energy Mater.*, 2017, **7**, 1602463.
62 Y. Pan, K. Sun, S. Liu, X. Cao, K. Wu, W. C. Cheong, Z. Chen, Y. Wang, Y. Li, Y. Liu, D. Wang, Q. Peng, C. Chen and Y. Li, *J. Am. Chem. Soc.*, 2018, **140**, 2610–2618.

63 L. Zeng, K. Sun, X. Wang, Y. Liu, Y. Pan, Z. Liu and D. Cao, *Nano Energy*, 2018, **51**, 26–36.
64 L. Hui, D. Jia, H. Yu, Y. Xue and Y. Li, *ACS Appl. Mater. Interfaces*, 2018, DOI: 10.1021/acsami.8b01887.
65 G. Zhang, Y. S. Feng, W. T. Lu, D. He, C. Y. Wang, Y. K. Li, X. Y. Wang and F. F. Cao, *ACS Catal.*, 2018, **8**, 5431–5441.
66 Y. Sun, C. Liu, D. C. Grauer, J. Yano, J. R. Long, P. Yang and C. J. Chang, *J. Am. Chem. Soc.*, 2013, **135**, 17699–17702.
67 C. L. Fan, D. L. Piron, A. Sleb and P. Paradis, *J. Electrochem. Soc.*, 1994, **141**, 382–387.
68 M. S. Faber, R. Dziedzic, M. A. Lukowski, N. S. Kaiser, Q. Ding and S. Jin, *J. Am. Chem. Soc.*, 2014, **136**, 10053–10061.
69 H.-W. Liang, S. Brüller, R. Dong, J. Zhang, X. Feng and K. Müllen, *Nat. Commun.*, 2015, **6**, 7992.
70 L. Liao, S. Wang, J. Xiao, X. Bian, Y. Zhang, M. D. Scanlon, X. Hu, Y. Tang, B. Liu and H. H. Girault, *Energy Environ. Sci.*, 2014, **7**, 387–392.
71 C. Hu, Q. Ma, S.-F. Hung, Z.-N. Chen, D. Ou, B. Ren, H. M. Chen, G. Fu and N. Zheng, *Chem*, 2017, **3**, 122–133.
72 Z.-Y. Yu, Y. Duan, M.-R. Gao, C.-C. Lang, Y.-R. Zheng and S.-H. Yu, *Chem. Sci.*, 2017, **8**, 968–973.
73 L. Fang, W. Li, Y. Guan, Y. Feng, H. Zhang, S. Wang and Y. Wang, *Adv. Funct. Mater.*, 2017, **27**, 1701008.
74 R. Zhang, P. A. Russo, M. Feist, P. Amsalem, N. Koch and N. Pinna, *ACS Appl. Mater. Interfaces*, 2017, **9**, 14013–14022.
75 J. Luo, *Science,* 2014, **345**, 1593–1596.
76 Q. Dong, C. Sun, Z. Dai, X. Zang and X. Dong, *ChemCatChem*, 2016, **8**, 3484–3489.
77 L. Feng, H. Vrubel, M. Bensimon and X. Hu, *Phys. Chem. Chem. Phys.*, 2014, **16**, 5917.
78 D. Liu, Q. Lu, Y. Luo, X. Sun and A. M. Asiri, *Nanoscale*, 2015, **7**, 15122–15126.
79 X. Zou, X. Huang, A. Goswami, R. Silva, B. R. Sathe, E. Mikmeková and T. Asefa, *Angew. Chemie - Int. Ed.*, 2014, **53**, 4372–4376.
80 J. Tian, Q. Liu, A. M. Asiri and X. Sun, *J. Am. Chem. Soc.*, 2014, **136**, 7587–7590.
81 H. Bin Wu, B. Y. Xia, L. Yu, X. Y. Yu and X. W. Lou, *Nat. Commun.*, 2015, **6**, 6512.
82 A. P. Grosvenor, B. A. Kobe, M. C. Biesinger and N. S. McIntyre, *Surf. Interface Anal.*, 2004, **36**, 1564–1574.
83 H. Wu, G. Gao, X. Zhou, Y. Zhang and S. Guo, *CrystEngComm*, 2012, **14**, 499–504.
84 P. W. Menezes, A. Indra, A. Bergmann, P. Chernev, C. Walter, H. Dau, P. Strasser and M. Driess, *J. Mater. Chem. A*, 2016, **4**, 10014–10022.
85 P. W. Menezes, A. Indra, D. González-Flores, N. R. Sahraie, I. Zaharieva, M. Schwarze, P. Strasser, H. Dau and M. Driess, *ACS Catal.*, 2015, **5**, 2017–2027.